Cell Reports

Article

Noradrenergic control of bone marrow and thymus by AgRP neurons is impaired in experimental multiple sclerosis

Graphical abstract

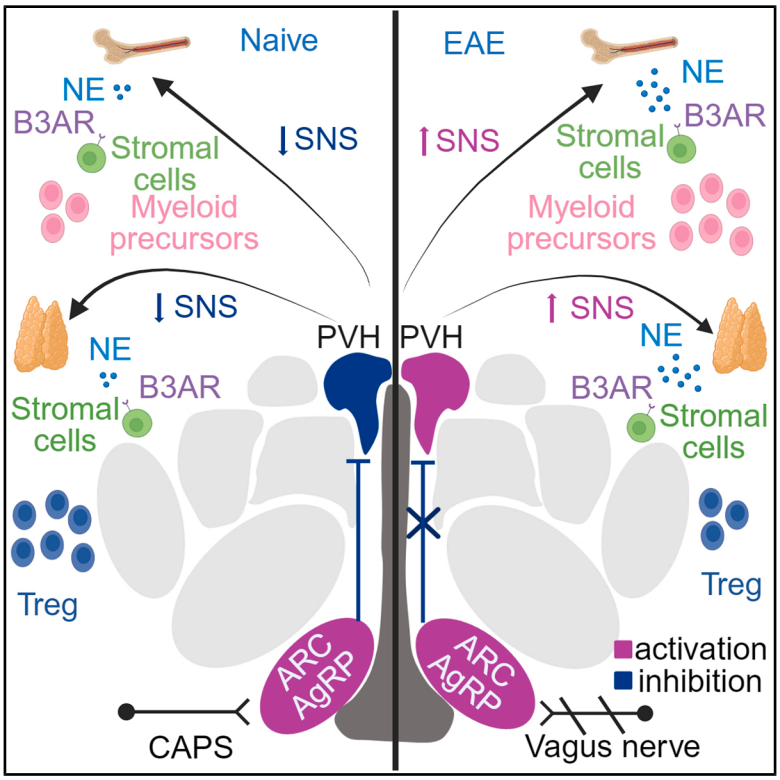

Highlights

- In EAE, NE promotes myeloid hematopoiesis and regulates Treg via B3ARs
- AgRP neurons modulate NE and B3ARs in BM and thymus
- AgRP neurons are dysfunctional in EAE
- Elevated serum levels of AgRP correlate with disease severity in people with MS

Authors

Tiziana Vigo, Maria C. Mariani, Caterina Bason, ..., Tamas L. Horvath, Nicole Kerlero de Rosbo, Antonio Uccelli

Correspondence

tiziana.vigo@hsanmartino.it (T.V.), auccelli@neurologia.unige.it (A.U.)

In brief

In this work, Vigo et al. demonstrate that norepinephrine (NE) promotes myeloid hematopoiesis in BM and regulates thymic Tregs via B3ARs in EAE. B3ARs are controlled by hypothalamic AgRP neurons, which are dysfunctional in EAE. Serum levels of AgRP are elevated in people with MS and correlate with disease severity.

Vigo et al., 2025, Cell Reports *44*, 116556
November 25, 2025
https://doi.org/10.1016/j.celrep.2025.116556

CellPress

Cell Reports

CellPress
OPEN ACCESS

Article

Noradrenergic control of bone marrow and thymus by AgRP neurons is impaired in experimental multiple sclerosis

Tiziana Vigo,[1,17,*] Maria C. Mariani,[1,2] Caterina Bason,[1] Giovanni Ferrara,[1] Eleonora Cornacchia,[2] Simona Francia,[1] Alberto Potenzieri,[1,2] Erika Ricci,[1] Giorgio Grasselli,[1,3] Gabriele Zoppoli,[1,4] Gabriella Cirmena,[4] Lorenzo Ferrando,[1] Claudio Procaccini,[5,6] Claudia Russo,[5,7] Tiziana Altosole,[1] Elena Cerutti,[1] Giovanna Capodivento,[1] Marta Bottero,[8] Luca Liberale,[1,4] Marco Scotto,[9] Alice Laroni,[1,2] Matilde Inglese,[1,2] Sebastian Sulis Sato,[1] Jonatas Catarino,[10] Diego Centonze,[11,12] Giuseppe Matarese,[5,13] Fabio Benfenati,[1,14] Tamas L. Horvath,[15] Nicole Kerlero de Rosbo,[2] and Antonio Uccelli[1,2,16,*]

[1]IRCCS Ospedale Policlinico San Martino, 16132 Genoa, Italy
[2]Department of Neurosciences, Rehabilitation, Ophthalmology, Genetics, Maternal and Child Health, University of Genoa, 16132 Genoa, Italy
[3]Department of Pharmacy, University of Genoa, 16132 Genoa, Italy
[4]Department of Internal Medicine and Medical Specialties, University of Genoa, 16132 Genoa, Italy
[5]Laboratory of Immunology, Institute of Endotypes in Oncology, Metabolism and Immunology "G. Salvatore," National Research Council, 80131 Naples, Italy
[6]Unit of Neuroimmunology, IRCCS Fondazione Santa Lucia, 00179 Roma, Italy
[7]Azienda Ospedaliera Universitaria "Federico II," 80138 Naples, Italy
[8]Department of Experimental Medicine, University of Genoa, 16132 Genoa, Italy
[9]Italian Institute of Technology, Nikon Imaging Center, 16163 Genoa, Italy
[10]Max Plank Institute for Metabolism Research, 50931 Koln, Germany
[11]Unit of Neurology, IRCCS Neuromed, 86077 Pozzilli, Italy
[12]Department of Systems Medicine, Tor Vergata University, 00133 Rome, Italy
[13]Treg Cell Lab, Department of Molecular Medicine and Medical Biotechnologies, University of Naples "Federico II," 80138 Naples, Italy
[14]Italian Institute of Technology, Center for Synaptic Neuroscience and Technology, 16132 Genoa, Italy
[15]Department of Comparative Medicine, Yale University School of Medicine, New Haven, CT 06520, USA
[16]Senior author
[17]Lead contact
*Correspondence: tiziana.vigo@hsanmartino.it (T.V.), auccelli@neurologia.unige.it (A.U.)
https://doi.org/10.1016/j.celrep.2025.116556

SUMMARY

Maturation of hematopoietic stem and progenitor cells (HSPCs) in the bone marrow (BM) and of T lymphocytes in the thymus occurs within stromal regions innervated by noradrenergic fibers of the sympathetic nervous system (SNS). However, the neuronal pathways governing noradrenergic activity in lymphoid organs remain largely unexplored. In experimental autoimmune encephalomyelitis (EAE), a mouse model of multiple sclerosis (MS), we demonstrated that noradrenergic signals promote myeloid hematopoiesis in the BM and regulate the intra-thymic frequency of regulatory T lymphocytes via β-3 adrenergic receptors (B3ARs). We further showed that B3ARs in the BM and thymus are controlled by hypothalamic neurons expressing agouti-related protein (AgRP), which are dysfunctional in EAE. Notably, elevated serum levels of AgRP correlate with disease severity and magnetic resonance imaging markers of neuroinflammation in people with MS. These findings reveal a mechanism of immune regulation mediated by noradrenergic transmission, offering potential therapeutic targets for immune-mediated diseases.

INTRODUCTION

In the bone marrow (BM), neural signals transmitted by the sympathetic nervous system (SNS), which are required for survival, expansion, and mobilization of hematopoietic stem and progenitor cells (HSPCs),[1] are mediated by norepinephrine (NE) through adrenergic receptors (ARs).[2] β-3 ARs (B3ARs) are expressed in the endosteal niche[3] and in the BM stroma by perivascular nestin-positive mesenchymal stromal cells (MSCs) that can differentiate into adipocytes and osteocytes,[4] and their activation contributes to the circadian mobilization of HSPCs.[2] Adrenergic activation of MSCs downregulates genes coding for factors involved in HSPC retention and differentiation, such as C-X-C motif chemokine ligand 12 (*Cxcl12*), vascular cell adhesion molecule 1 (*Vcam1*), c-kit ligand (*KitL*), angiopoietin 1 (*Angpt1*), and interleukin 7 (*Il-7*).[4] Pharmacological modulation of B3ARs restored normal hematopoiesis in experimental models of aging,[5] diabetes,[6] myeloid malignancies,[7] stroke, intracerebral hemorrhage, and stress.[8–10]

Similar to the BM, where stromal niches drive the maturation of particular immune lineages,[11] the thymus is composed of spatially discrete stromal areas that contribute to distinct developmental trajectories of lymphoid progenitors.[12] The thymus receives extensive sympathetic innervation,[13] and *Cxcl12* is expressed in the cortex of the thymus by cortical epithelial cells.[14]

Sympathetic fibers connecting the brain to the BM and thymus originate in several hypothalamic nuclei, including the paraventricular (PVH) and the arcuate (Arc) nucleus[15,16]. Agouti-related protein (AgRP)-expressing neurons in the Arc normally suppress sympathetic activity via the PVH[17] and are known for their role in feeding and energy balance.[18] However, studies in AgRP-Sirt1$^{-/-}$ mice, which display hypofunctional AgRP neurons, revealed that these neurons also influence the BM and thymus.[19,20] These mice display high levels of NE in the BM and osteopenia, which can be mitigated by B3AR blockade.[20] This suggests that AgRP neurons may target bone progenitors, such as MSCs, within the hematopoietic niche via the SNS and influence their differentiation through B3AR. AgRP-Sirt1$^{-/-}$ mice also exhibit an immature thymic phenotype and generate a low percentage of regulatory T lymphocytes (Tregs). This results in inadequate control of autoreactive T cells associated with increased susceptibility to experimental autoimmune encephalomyelitis (EAE), a model for multiple sclerosis (MS),[21] supporting a role for AgRP neurons in the control of thymic function. Moreover, in transgenic mice in which the expression of the transient receptor potential vanilloid 1 (TRPV1) is restricted to AgRP-cre neurons (AgRP-TRPV1 mice),[22] activation of these neurons by capsaicin (CAPS) reduces the activation of B3ARs in fat, impacting energy balance.[23] Cellular energy metabolism of immune cells is a critical determinant of their adaptations and functions.[24,25] The hematopoietic niche is characterized by unique metabolic features that control HSPC maintenance and function.[26] These premises suggest that neurons involved in regulating energy metabolism, AgRP neurons, may also be relevant in hematopoiesis, which was recently reported to be altered during EAE.[27,28]

Here, we investigate the interplay between hypothalamic AgRP neurons and the SNS in the BM and thymus during EAE. Our study reveals that AgRP neurons modulate signals transmitted through the SNS to influence both hematopoiesis and the intra-thymic Treg cell compartment and that they are dysfunctional in EAE. We also demonstrate that the AgRP neuropeptide is increased in the serum of people with MS (pwMS), and its levels correlate with clinical disability and neuroinflammation, suggesting its potential role as a biomarker in MS.

RESULTS

Changes in hematopoiesis and T cell lymphopoiesis in EAE are associated with increased NE in BM and thymus

To assess whether EAE results in modulation of adrenergic transmission in the femur BM, we quantified NE at various days post-immunization (dpi) with the encephalitogenic peptide of myelin oligodendrocyte protein ($MOG_{35–55}$), corresponding to the presymptomatic (7 dpi), acute (15 dpi), and chronic (25 dpi) phases of the disease (Figures S1A and S1B). We observed that NE levels were significantly increased at 7 and 15 dpi and dropped at 25 dpi compared to the naive condition (0 dpi; Figure 1A). In parallel with the rise in NE, we found an increased expression of tyrosine hydroxylase (TH), the key enzyme involved in the synthesis of NE (Figures 1B and 1C). The expression of genes (*Cxcl12*, *Vcam1*, *Angpt1*, *KitL*, and *Il7*) that have been previously demonstrated to be down-regulated upon adrenergic activation of the hematopoietic niche[4] was found to be reduced in EAE mice at all analyzed time points (Figure 1D). Such effect was completely abrogated by femoral and sciatic denervation (Figure 1D, column D), demonstrating that the hematopoietic niche is activated by SNS signals in EAE. The increase in NE in the BM was associated with changes in HSPCs and immune cells (gating strategy in Figures S2A and S2B). The frequency of Lin$^-$/Sca-1$^+$/c-Kit$^+$ (LSK) precursor cells, an early form of HSPCs, increased at 7 and 15 dpi and was restored at 25 dpi compared to naive mice (Figure 1E). Similar changes were observed in the absolute cell number of LSK cells (Figure S2C). To identify the molecular signatures modulated in BM cells upon EAE induction, we performed bulk RNA-sequencing (RNA-seq) analysis on Lin$^-$/Sca-1$^+$ stem cells isolated from the BM of either naive or EAE mice (7 dpi). Gene set enrichment analysis (GSEA) of differentially expressed genes (DEGs) between the two experimental groups revealed, in EAE, a positive normalized enrichment score (NES) for pathways involved in oxidative phosphorylation, proliferation (DNA replication and cell cycle), osteoclast differentiation, and inflammation (IL-17 and TNF signaling, cytokine-cytokine receptor interaction, chemokine signaling, Myc pathway, C-type lectin receptor, and NOD-like receptor signaling; Figure 1F; Table S1). A negative NES of Wnt and Hedgehog pathways, involved in self-renewal and differentiation of stem cells, epithelial-to-mesenchymal transition (EMT), and cell contacts (cell adhesion, extracellular matrix [ECM]-receptor interaction, tight junctions, and focal adhesions), was observed (Figure 1F; Table S1). Then, we assessed the commitment of undifferentiated LSK cells through flow cytometric analysis of myeloid progenitors (MPs; Lin$^-$/Sca-1$^-$/c-Kit$^+$/CD34$^+$), which include both common myeloid progenitors and granulocyte-monocyte progenitors, and of common lymphoid precursors (CLPs; Lin$^-$/Sca-1$^+$/c-Kit$^+$/CD127$^+$/CD135$^+$). The frequency of MPs increased at both at 7 and 15 dpi and was reduced at 25 dpi (Figure 1G), while the frequency of CLPs did not significantly change (Figure 1G) during the different stages of EAE. These modifications were paralleled by an increase in the frequency of neutrophils (Neutro; CD45$^+$/Cd11b$^+$/Ly6C$^+$/Ly6G^{hi}) and monocytes (Mono; CD45$^+$/Cd11b$^+$/Ly6C$^+$/Ly6G$^-$) and by a reduction of B lymphocytes (CD45$^+$/CD11b$^-$/CD19$^+$), while T lymphocytes (CD45$^+$/CD11b$^-$/CD19$^-$/CD3$^+$) remained unaltered (Figure 1H). Similar changes were observed in the absolute numbers of MPs and immune cells (Figures S2C and S2D). In peripheral blood, Neutro increased at 7 and 15 dpi and returned to basal levels at 25 dpi, B lymphocytes decreased at all time points, and Mono and T lymphocytes remained unchanged (Figure 1I). These data indicated that a myeloid bias of hematopoiesis occurs in EAE, as previously reported.[27] Control mice immunized with complete Freund's adjuvant (CFA) in the absence of the encephalitogenic peptide did not develop the disease but still displayed an increase in NE (Figure S3A) and in the frequency and absolute numbers of LSK cells and MPs at 7 dpi (Figures S3B and S3C); however, all these parameters returned to basal levels at 15 dpi (Figures S3A–S3C). In line with evidence showing that HSPCs mobilized from the BM sustain thymic

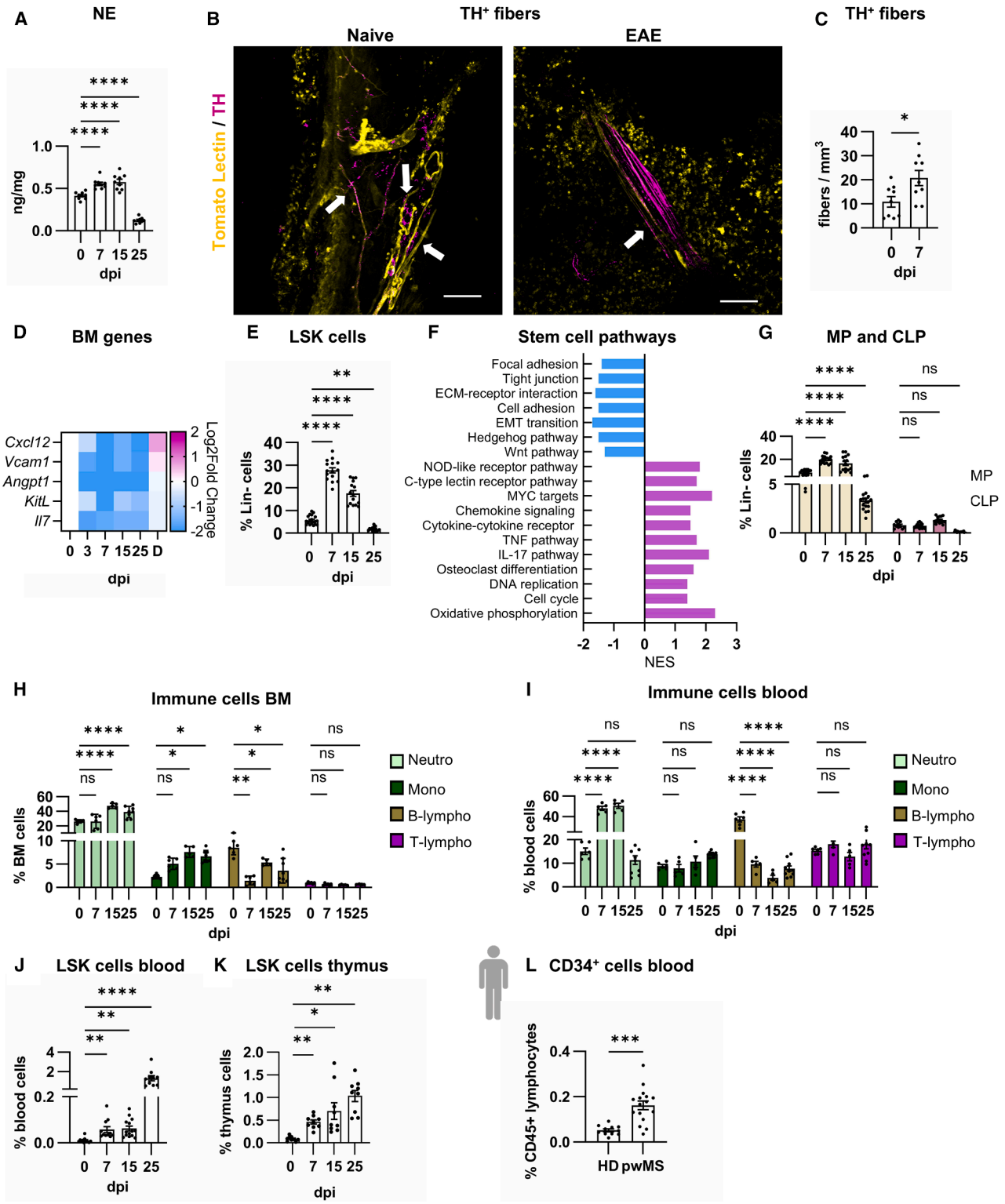

Figure 1. Altered adrenergic signaling, gene expression profile, and cellular composition of the BM in EAE

(A–K) C57BL/6 naive and EAE mice, clinical scores (mean ± sem): 15 dpi (2.6 ± 0.265) and 25 dpi (2.03 ± 0.285). (A) Concentration of NE in the BM; $n = 9$ mice per group. (B) TH$^+$ fibers (magenta, indicated by white arrows) in BM. Scale bars, 50 μm. (C) Density of TH$^+$ fibers in the BM; $n = 3$ mice per group, 3 images per mouse. (D) Gene expression in the BM. Data are log2 fold change of EAE (7 dpi) vs. naive mice; $n = 9$ mice per group. Denervated (D) mice ($n = 5$) were operated 10 days before immunization. (E) Frequency of LSK cells in BM; $n = 15$ mice per group. (F) Normalized enrichment scores (NES) of the gene pathways in BM Lin$^-$/Sca-1$^+$ cells from EAE

(legend continued on next page)

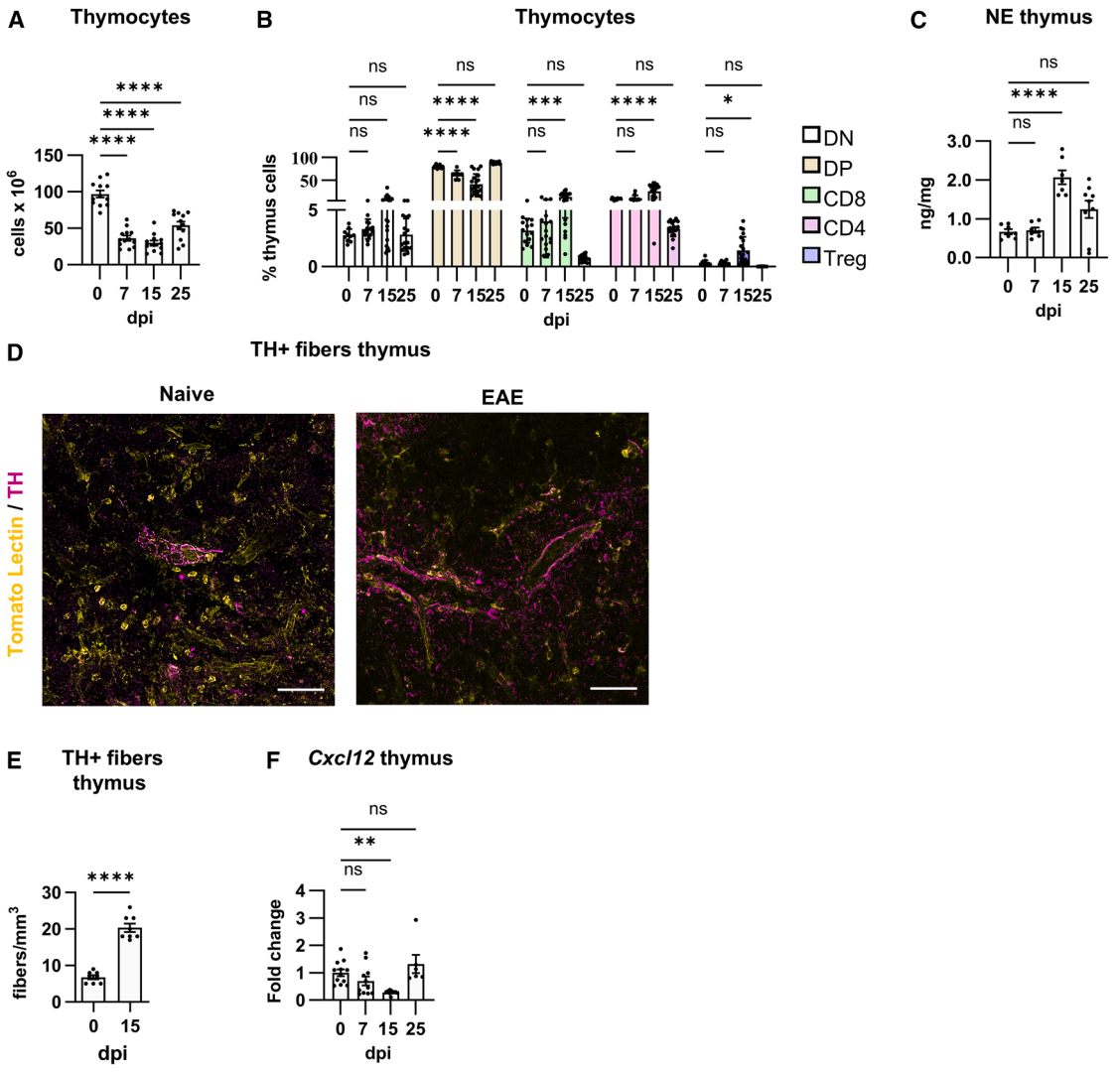

Figure 2. Altered adrenergic signaling, gene expression, and cellular composition of the thymus in EAE

C57BL/6 naive and EAE mice, clinical scores (mean ± sem): 15 dpi (2.6 ± 0.265) and 25 dpi (2.03 ± 0.285).

(A) Number of thymus cells; $n = 12$ per group.

(B) Frequency of thymocytes; $n = 15$ mice per group.

(C) Concentration of NE in thymus; $n = 7$ mice per group.

(D) TH^+ fibers in the thymus (in magenta). Scale bars, 50 μm.

(E) Density of TH^+ fibers in the thymus; $n = 3$ mice per group, 3 images per mouse.

(F) Gene expression of *Cxcl12* in the thymus. Data are fold change vs. naive condition; $n = 6$–15 mice per group. Error bars are mean ± sem. Data points indicate independent mice.

$^*p < 0.05$, $^{**}p < 0.01$, $^{***}p < 0.001$, $^{****}p < 0.0001$, ns = not significant by one-way ANOVA/Tukey's test (A, C, and F), two-way ANOVA/Dunnett's test (B), or unpaired Student's *t* test (E). See also Figures S4C–S4G and S5.

maturation of T cells,[29] we observed an increase in LSK precursor cells in the peripheral blood (Figure 1J) and in the thymus (Figures 1K and S4A). We also found an increased frequency of $CD34^+$ cells in the peripheral blood of pwMS compared with healthy donors (HDs; Figure 1L, gating strategy in S4B), confirming that mobilization of HSPCs also occurs in the human disease.

Given the observed increase in LSK cells in the thymus of EAE mice, we proceeded to assess the intra-thymic maturation of

(7 dpi) vs. naive mice; $n = 3$ mice per group. (G–L) Frequency of (G) MPs and CLPs in the BM; $n = 15$ mice per group. (H) $CD45^+$ cells in the BM; $n = 6$ mice per group. (I) $CD45^+$ cells in peripheral blood; $n = 6$ mice per group. (J) LSK cells in peripheral blood; $n = 12$ mice per group. (K) LSK cells in the thymus; $n = 9$ mice per group. (L) $CD34^+$ cells in peripheral blood of 11 HDs and 16 pwMS. Error bars are mean ± sem. Data points indicate independent mice or human samples.

$^*p < 0.05$, $^{**}p < 0.01$, $^{***}p < 0.001$, $^{****}p < 0.0001$, ns = not significant by one-way ANOVA/Tukey's test (A, E, J, and K), two-way ANOVA/Dunnett's test (G–I), and unpaired Student's *t* test (C and L). See also Figures S1–S3, S4A, and Tables S1 and S2.

T cells (gating strategy in Figure S4C). First, we observed that the number of thymocytes significantly decreased across all phases of EAE (Figure 2A). There was an increase in the frequency (Figure 2B) and absolute numbers (Figures S4D–S4G) of single-positive CD8, CD4, and Treg cells and a reduction of intermediate double-positive (DP) precursors at 15 dpi. Additionally, NE increased at 15 dpi (Figure 2C), together with the number of TH+ fibers (Figures 2D and 2E). Concomitant with the increase in NE, the expression of *Cxcl12* was reduced at 15 dpi and restored at 25 dpi (Figure 2F). Control mice immunized with CFA did not display any change in the levels of NE in the thymus (Figure S5A); however, they still showed a reduced frequency of DP precursors and an increase in $CD4^+$ and $CD8^+$ cells at 7 dpi, whereas at 15 dpi, thymic subsets returned to basal levels (Figure S5B).

Chemogenetic activation of AgRP-cre neurons reduces NE in the BM and thymus, restricts myeloid hematopoiesis, and increases Tregs in the thymus

In AgRP-TRPV1 mice, intraperitoneal injection of CAPS results in the chemogenetic activation of AgRP-cre neurons occurring within 1 h after CAPS administration.[22] As a consequence of chemogenetic stimulation, the expression of the *Agrp* gene increased in the hypothalamus, peaking 8 h after CAPS injection and returning to basal levels after 24 h (Figure 3A). Cell bodies of AgRP-cre neurons lie in the Arc, while many of their axons project to the PVH (Figure 3B), a hypothalamic center regulating the activity of the SNS.[17] As expected, upon intraperitoneal injection of CAPS, the number of nuclei positive for c-FOS, a marker of neuronal activation, increased in the AgRP-positive area of the Arc (Figures 3C and 3D). In parallel, we observed a significant reduction of c-FOS+ nuclei in the AgRP-positive area of the PVH (Figures 3E and 3F), likely due to the inhibitory effect of AgRP neurons on the PVH.[30,31]

Following CAPS injection, we observed a reduction in NE levels in the BM (Figure 3G), which was associated with an increased expression of *Cxcl12* (Figure 3H). After 3 days of daily CAPS administration, the frequency (Figures 3I and 3J) and absolute numbers (Figures S6A and S6B) of MPs and Neutro in the BM of AgRP-TRPV1 mice were reduced. In the thymus, chemogenetic activation of AgRP-cre neurons also resulted in a significant reduction in NE (Figure 3K) and a parallel increase in *Cxcl12* expression (Figure 3L). Daily CAPS injection for 3 days did not induce changes in thymic subsets, except for the frequency (Figure 3M) and absolute number (Figure S6C) of Tregs, which was significantly increased. These observations indicate that AgRP-cre neurons control SNS transmission in BM and thymus, with effects on hematopoiesis and Tregs.

To further confirm the effect of AgRP neuron stimulation on the BM and thymus, we utilized a DREADD model of chemogenetic activation of AgRP neurons, achieved by injecting AgRP-ires-cre mice with a cre-dependent adeno-associated virus (AAV) carrying the hM3Dq receptor and the mCherry reporter (AgRP-hM3Dq mice[32]; Figure S7A). After 3 days of clozapine N-oxide (CNO) administration, we observed a reduction of MPs and Neutro in the BM (Figures S7B and S7C) and an increase of Tregs in the thymus (Figure S7D). Prolonged stimulation of AgRP-cre neurons also resulted in a significant increase in body weight (Figure S7E), as previously reported.[33]

Chemogenetic activation of AgRP-cre neurons mimics the effect of inhibition of B3ARs in the BM and thymus

Given that the chemogenetic activation of AgRP-cre neurons was sufficient to alter the levels of NE, the expression *Cxcl12* and the frequency of HPSCs in the BM, we postulated that B3ARs, key mediators of the interplay between NE and the hematopoietic niche, were involved in this process. We confirmed that B3ARs are expressed in the BM by MSCs (identified as Lin^-/$Sca\text{-}1^+$/$CD73^+$ BM cells; Figures S8A and S8B), as well as by primary cultures of BM-derived MSCs (Figure S8C). We observed that B3ARs were not expressed in neutrophils, monocytes, B lymphocytes, and T lymphocytes in the BM (Figure S8D). Then, we compared the effects of the chemogenetic activation of AgRP-cre neurons with those of the chemical modulation of B3ARs on the expression of *Cxcl12*. Similar to CAPS, the administration of the B3AR antagonist SR59230A (SR) resulted in increased *Cxcl12* expression, which was blunted by the co-administration of CAPS with the B3AR agonist CL316.243 (CL) (Figure 4A). Then we compared the effect of CAPS with that of B3AR modulation (achieved by SR, CL, and CL + CAPS treatments) on MPs. Both CAPS and the antagonist of B3ARs SR reduced the frequency of MPs (Figure 4B) and their absolute number (Figure S8E). The B3AR agonist CL did not exert any effect on MPs but abrogated the effect of CAPS when co-administered (Figures 4B; S8E). Altogether, these results indicate that the chemogenetic activation of AgRP-cre neurons mimics the effect of inhibition of B3ARs in the BM.

In the thymus, we observed that B3ARs were expressed in cortical and sub-cortical areas (Figure 4C). Remarkably, both cortical epithelial cells (cTECs), which are known to express *Cxcl12*,[14] and medullary epithelial cells (mTECs) (gating strategy in Figure S9A), expressed B3ARs (Figure 4D), differently from $CD3^+$ cell subsets that did not express B3ARs (Figure S9B). Then, we compared the effect of CAPS and the modulators of B3ARs in the thymus. Both CAPS and the B3AR antagonist SR increased the expression of *Cxcl12* (Figure 4E). When administered together with the B3AR agonist CL, the effect of CAPS was completely abrogated (Figure 4E). Then, we compared the effect of CAPS with that of SR, CL, and CL + CAPS on Tregs. Both CAPS and the antagonist of B3ARs SR increased the frequency of Tregs (Figure 4F), while the B3AR agonist CL did not exert any effect on Tregs but completely abrogated that of CAPS when administered together (Figure 4F). Similar results were obtained considering the absolute cell number of Tregs in the thymus (Figure S9C). The chemogenetic activation of AgRP-cre neurons, as well as the inhibition of B3ARs with SR, increased the expression of *Il-15* (Figure 4G), a chemokine produced by TECs that promotes the maturation of Tregs.[34] Altogether, these results indicate that the chemogenetic activation of AgRP-cre neurons mimics the effect of inhibition of B3ARs also in the thymus.

Pharmacological inhibition of B3ARs ameliorates EAE

To understand whether B3ARs were implicated in the changes observed in hematopoiesis and thymopoiesis during EAE, we assessed the effect of the B3AR antagonist on the BM and thymus. Administration of SR from the day of immunization significantly reduced the frequency of LSK cells at 7 dpi

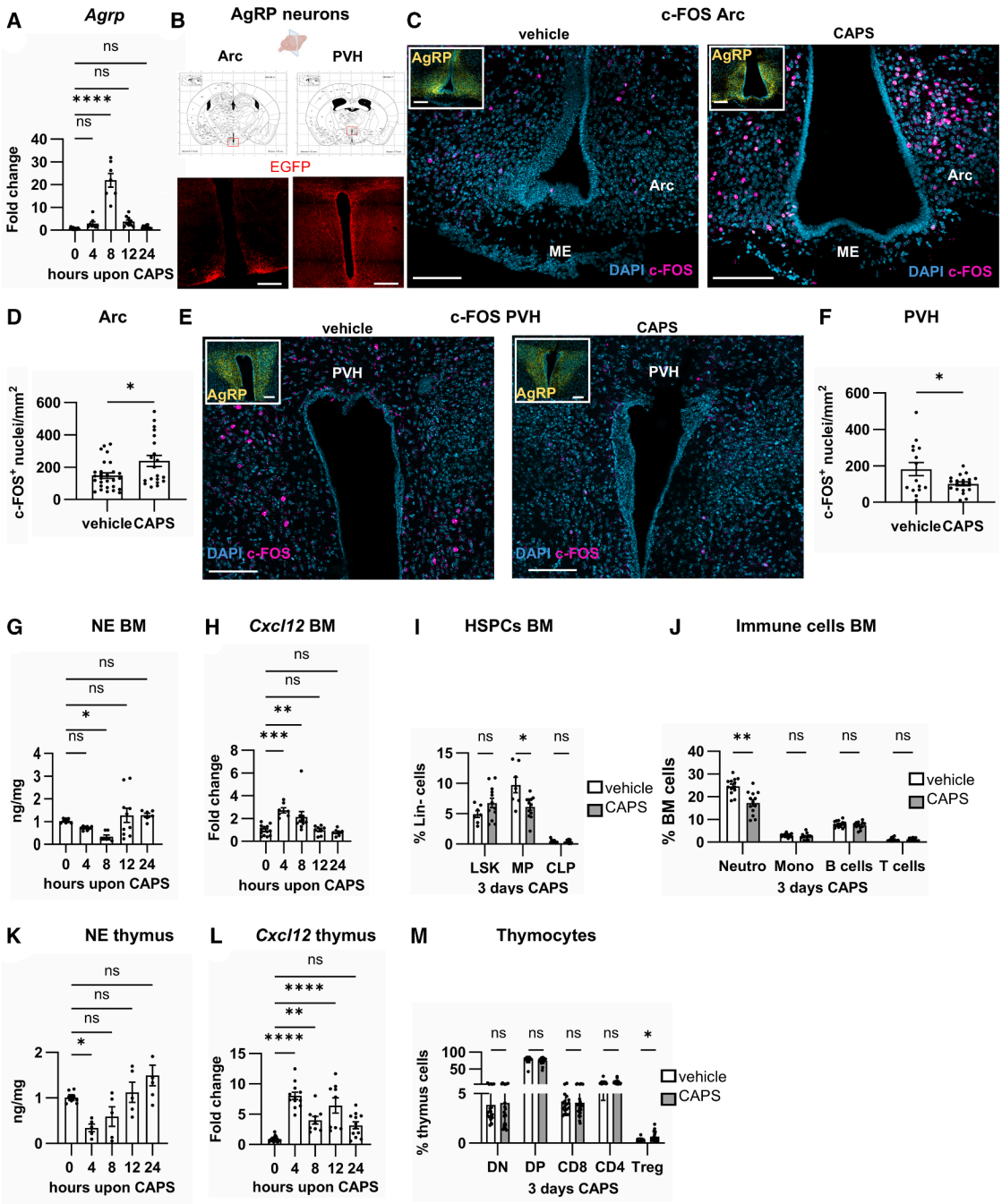

Figure 3. Chemogenetic activation of AgRP-cre neurons alters adrenergic signaling, gene expression, and cellular composition in the BM and thymus

AgRP-TRPV1 naive mice. (A) Gene expression of *Agrp* in hypothalamus extracts. Data are fold change vs. vehicle; $n = 7–16$ per group. (B) EGFP+ cell bodies in the Arc and projections in the PVH of AgRP-EGFP mice. Scale bars, 100 μm. (C) Immunolabeling for AgRP (yellow in the low-magnification images) and c-FOS (magenta in the high-magnification images) in the Arc. Nuclei were counterstained with DAPI (cyan). Scale bars, 100 μm. (D) Quantification of c-FOS+ nuclei in the AgRP+ area of the Arc; $n = 13–8$ slices from 3 mice per group. (E) Immunolabeling for AgRP (yellow in the low-magnification images) and c-FOS (magenta in the high-magnification images) in the PVH. Nuclei were counterstained with DAPI (cyan). Scale bars, 100 μm. (F) Quantification of c-FOS+ nuclei in the AgRP+ area of the PVH; $n = 13–8$ slices from 3 mice per group (G) Concentration of NE in the BM; $n = 6–10$ per group. (H) Gene expression of *Cxcl12* in the BM. Data are fold change vs. vehicle; $n = 7–13$ per group. (I) Frequency of HSPCs in the BM; $n = 7–11$ per group. (J) Frequency of immune cells in the BM; $n = 11–13$ per group. (K) Concentration of NE in the thymus; $n = 5–8$ per group. (L) Gene expression of *Cxcl12*. Data are fold change vs. vehicle; $n = 8–12$ per group. (M) Frequency of thymocytes; $n = 18–30$ per group. Error bars are mean ± sem. Data points indicate independent mice (A and G–M) or brain slices (D and F).

$^*p < 0.05$, $^{**}p < 0.01$, $^{***}p < 0.001$ $^{****}p < 0.0001$; ns = not significant by one-way ANOVA/Tukey's test (A, G, H, K, and L), unpaired *t* test (D and F), multiple unpaired Student's *t* tests (I, J, and M). See also Figures S6 and S7.

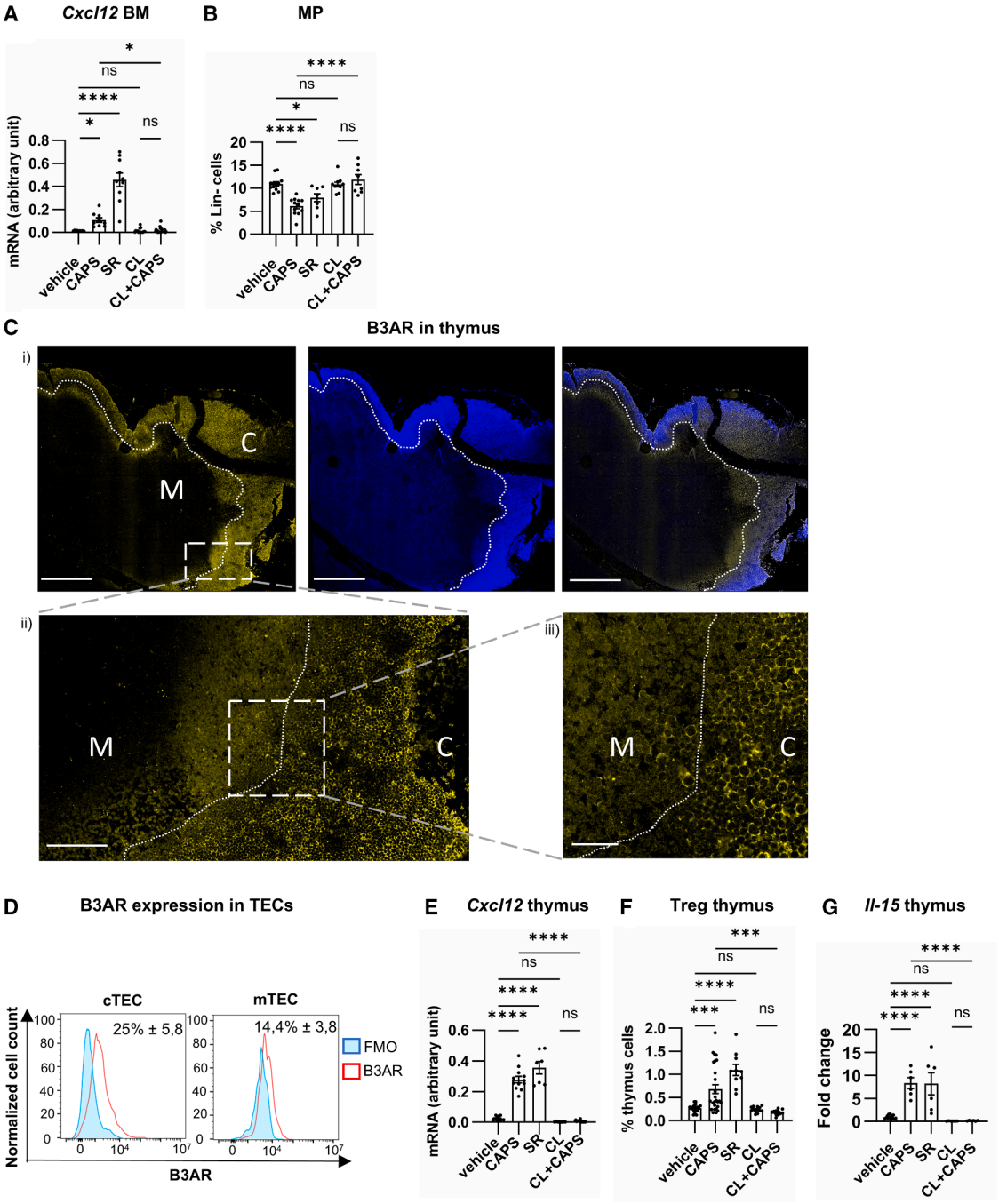

Figure 4. Chemogenetic activation of AgRP-cre neurons mimics the effect of B3AR blockade on the BM and thymus

(A and B) AgRP-TRPV1 naive mice. (A) Gene expression of *Cxcl12* in BM 4 h after injection of CAPS, SR, CL, or CL + CAPS. CL was administered 1 h before CAPS; $n = 9–15$ mice per group. (B) Frequency of MP in BM after 3 days of CAPS, SR, CL, or CL + CAPS; $n = 8–12$ mice per group.

(C and D) C57BL/6 naive mice. (C) B3ARs in the thymus. B3ARs (yellow), cell nuclei (blue), and merged channels. The thymus cortex (C) and medulla (M) are separated by dotted lines. Dashed lines identify the zoomed-in areas. Scale bars, 500 (i), 100 (ii), and 30 (iii). (D) Expression of B3ARs in cTEC and mTEC; $n = 5$ mice.

(E–G) AgRP-TRPV1 naive mice. (E) Gene expression of *Cxcl12* in thymus 4 h after injection of CAPS, SR, CL, or CL + CAPS. CL was administered 1 h before CAPS; $n = 8–15$ mice per group. (F) Frequency of Treg in the thymus after 3 days of CAPS, SR, CL, or CL + CAPS; $n = 11–25$ mice per group. (G) Gene expression of *Il-15* in the thymus 4 h after injection of CAPS, SR, CL, or CL + CAPS. CL was administered 1 h before CAPS; $n = 6$ mice per group. Error bars are mean ± sem. Data points indicate independent mice.

$^{*}p < 0.05$, $^{***}p < 0.001$; $^{****}p < 0.0001$; ns = not significant by one-way ANOVA/Tukey's test. See also Figures S8 and S9.

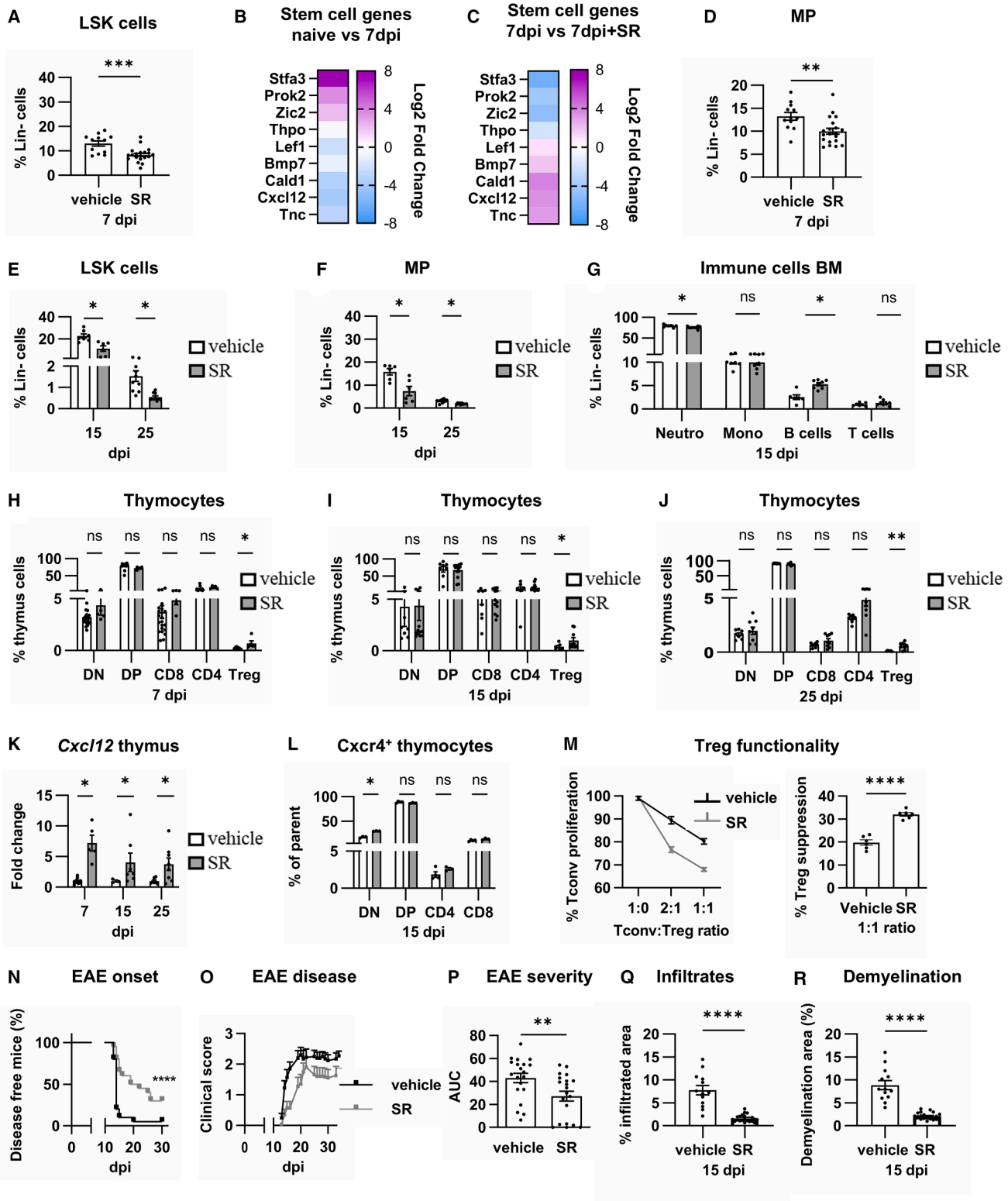

Figure 5. Pharmacological blockade of B3ARs changes the cellular composition of the BM and thymus and ameliorates EAE

C57BL/6 EAE mice. (A) Frequency of LSK cells in the BM at 7 dpi; *n* = 12–20 per group. (B) Gene expression of BM stem cells in naive vs. EAE mice. Data are log2 fold change; *n* = 3 mice per group. (C) Gene expression of BM stem cells in EAE vs. EAE treated with SR mice. Data are expressed as log2 fold change; *n* = 3 mice per group. Frequency of (D) MPs in the BM; *n* = 12–20 mice per group. (E) LSK cells in the BM; *n* = 6–10 mice per group. (F) MPs in the BM; *n* = 6–10 mice per group.

(legend continued on next page)

(Figure 5A). Comparison of the RNA-seq profile between naive and EAE-induced mice, treated or not with SR, indicated that SR mitigated the effect of EAE induction on the expression of genes involved in stem cell proliferation, differentiation, and mobilization. Indeed, genes that were up-regulated in EAE-induced mice, such as stefin A3 (*Stfa3*), prokinetikin 2 (*Prok2*), and zinc finger protein 2 (*Zic2*), or not modulated, as in the case of thrombopoietin (*Thpo*; Figure 5B), displayed reduced expression upon treatment (Figure 5C). Instead, genes coding for molecules involved in cell adhesion, tight junctions, and ECM-receptor interaction (like *Cxcl12,* caldesmon 1 [*Cald1*], and tenascin C [*Tnc*]) and for transcription factors important for HSPC differentiation (such as the lymphoid-enhancer binding factor 1 [*Lef1*] and bone morphogenetic protein 7 [*Bmp7*]), which were down-regulated in untreated mice (Figure 5B), displayed increased expression upon treatment (Figure 5C). Treatment with SR reduced the frequency of MPs in EAE-induced mice at 7 dpi (Figure 5D). A reduced frequency of both LSK cells and MP in the BM was also observed at 15 and 25 dpi (Figures 5E and 5F). The frequency of Neutro in the BM at the disease peak was significantly reduced, while that of B lymphocytes increased (Figure 5G), indicating that the pharmacological blockade of B3ARs was able to counteract the effects of EAE in the BM. Similar results were obtained considering the absolute numbers of BM cells (Figures S10A–S10C).

In the thymus, inhibition of B3ARs did not restore DN, DP, and $CD4^+$ and $CD8^+$ thymocytes but increased the frequency (Figures 5H–5J) and absolute number (Figure S10D) of Tregs. The gene expression of *Cxcl12* was augmented by the treatment (Figure 5K), and, in parallel, the frequency of DN precursors expressing Cxcr4, the receptor for Cxcl12, increased (Figure 5L). In addition to increasing the number of Tregs in the thymus, pharmacological inhibition of B3ARs enhanced the ability of peripheral Tregs to diminish the proliferation of conventional T lymphocytes (Tconv) in *in vitro* co-culture assays (Figure 5M). Concurrently, no difference in the proliferation of Tconv cells was observed (Figure S10E) when Tconv were cultured alone, suggesting a specific effect of the B3AR antagonist on the regulatory compartment during EAE.

The antagonist of B3ARs was able to significantly delay the onset of the disease (Figure 5N) and ameliorate the clinical course of EAE (Figures 5O, 5P, and S10F). The histological analysis of the spinal cord revealed a significant reduction of immune infiltrates and demyelination in treated mice (Figures 5Q and 5R; S10G).

AgRP neurons are dysfunctional in EAE

As the chemogenetic activation of AgRP-cre neurons in naive mice mimicked the effect of pharmacological inhibition of B3ARs, we used CAPS to reverse BM alterations and to increase Tregs in AgRP-TRPV1 mice immunized for EAE (Figure S11A). Unexpectedly, we observed that stimulation of AgRP-cre neurons with CAPS at 7 dpi did not reduce NE or augment the expression of *Cxcl12* in the BM and thymus and did not alter the frequency of BM HSPCs and thymus Tregs (Figures S11B–S11G). Administration of CAPS reduced, rather than increased, AgRP expression in the hypothalamus (Figure 6A). To investigate if this outcome might reflect changes in neuronal activity, we performed *in vivo* electrophysiology recordings in the Arc of both healthy and EAE AgRP-TRPV1 mice (7 dpi; Figures S11H and S11I). Interestingly, electrical activity in the Arc was increased in EAE-induced AgRP-TRPV1 mice (7 dpi) compared to naive mice (Figures 6B and 6C). Administration of CAPS induced a 2-fold increase in the firing frequency in the Arc of naive mice but did not further increase the spiking activity in EAE mice (Figure S11J). Even though *in vivo* electrophysiological recordings allowed only detection of extracellular electrical activity of multiple neuronal population, these data suggested a potential hyperactivity of AgRP neurons in EAE. This was further supported by increase in AgRP expression in the Arc (Figures 6D and S12A) and in c-FOS+ nuclei in the AgRP-positive area of the Arc (Figures 6E and S12B) in EAE wild-type mice.

Despite AgRP neurons showing signs of activation in EAE, we observed reduced AgRP expression (Figures 6F and S12C) and an increased number of $c\text{-}FOS^+$ nuclei in the AgRP-positive area of the PVH (Figures 6G and S12D). To evaluate whether a reduction in AgRP projection could account for this, we employed a viral approach by stereotaxically injecting AgRP-ires-Cre mice with a cre-dependent AAV carrying the EGFP reporter (AgRP-EGFP mice), allowing for genetic labeling of AgRP neurons in the Arc (Figure S13A) and of their projections in the PVH (Figure 6H, EGFP panel). Quantification showed a significant reduction of the EGFP-positive area in the PVH, normalized to the total number of $EGFP^+$ neurons in the Arc (Figure 6I), in EAE mice (7 dpi) compared to naive controls. Since most AgRP neurons are GABAergic, we performed immunostaining for vesicular GABA transporter (VGAT), a pre-synaptic marker of inhibitory terminals (Figure 6H, VGAT panel), and quantified its overlap with EGFP-labeled AgRP axons in the PVH (Figure 6H, binary EGFP and binary EGFP/VGAT panels). We observed a significant reduction of the $VGAT^+/EGFP^+$ area in EAE mice (7 dpi) compared to naive controls (Figure 6J). Altogether, these results suggested that EAE leads to a reduction of AgRP neuron projections, impairing their inhibitory control over the PVH. As neurons producing corticotropin-releasing factor (Crf) are also located in the PVH and are involved in the modulation of the SNS,[35,36] we investigated whether these neurons exhibit signs of alteration in EAE.

(G) Immune cells in the BM; $n = 7–8$ mice per group. (H–J) Frequency of thymocytes; $n = 5–15$ mice per group. (K) Gene expression of *Cxcl12* in the thymus. Data are fold change vs. control; $n = 5–8$ mice per group. (L) Frequency of Cxcr4+ thymocytes; $n = 4$ mice per group. (M) Left: proliferation of Tconv cells isolated from the spleens and cultured in the presence of autologous Treg cells at different ratios. *Right panel:* percentage of Treg suppressive activity in co-culture assays, reported in the left panel, at the Tconv/Treg ratio of 1:1; $n = 6$ values from 3 pools of mice in technical duplicates. (N) Kaplan-Meier analysis of disease onset; $n = 20$ mice per group. (O) Clinical course of EAE; $n = 20$ mice per group. (P) Quantification of the area under the curve (AUC) from 14 to 34 dpi; $n = 20$ mice per group. (Q) Immune infiltrates in the spinal cord; $n = 12$ slices from 4 mice per group. (R) Demyelination in the spinal cord; $n = 12$ slices from 4 mice per group. Error bars are mean ± sem. Data points indicate independent mice (A, D–L, N, and P), means (M and O), or slices (Q and R).

$^*p < 0.05$, $^{**}p < 0.01$, $^{***}p < 0.001$, $^{****}p < 0.0001$; ns = not significant by Student's *t* test (A, D, and P), Mann-Whitney (M, Q, and R), multiple unpaired *t* tests (E–L), and log rank test (N). See also Figure S10.

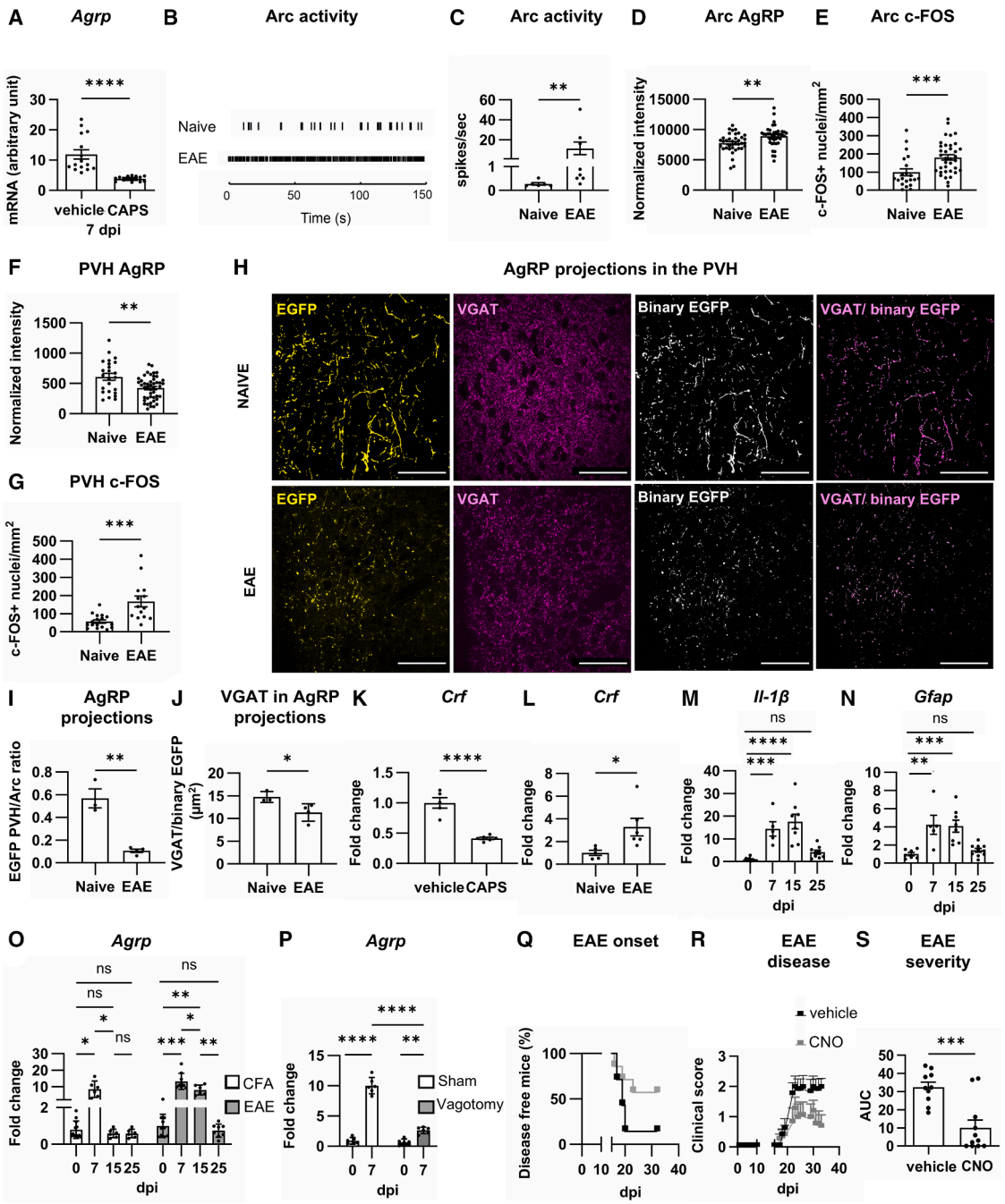

Figure 6. AgRP neurons are dysfunctional in EAE

(A–C) AgRP-TRPV1 naive and EAE mice (7 dpi): (A) Gene expression of *Agrp* after 7 days of CAPS. Data are arbitrary units ($2-\Delta CT$); $n = 15$ mice per group. (B) Raster plot of the extracellular recording of spike activity in the Arc. (C) Maximum firing rate (spikes/sec); $n = 5–8$ mice per group.

(D–G) C57BL/6 naive and EAE mice (7 dpi). (D) Intensity of AgRP immunofluorescence in the Arc; $n = 37–40$ slices from 4 mice per group. (E) Number of c-Fos+ nuclei in the AgRP+ area of the Arc; $n = 21–36$ slices from 4 mice per group. (F) Intensity of AgRP immunofluorescence in the PVH; $n = 37–40$ slices from 4 mice per group. (G) Number of c-Fos+ nuclei in the AgRP+ area of the PVH; $n = 17–14$ slices from 4 mice per group.

(H–J) AgRP-EGFP naive and EAE mice (7 dpi). (H) EGFP+ fibers and VGAT staining in the PVH before (EGFP and VGAT) and after analysis (binary EGFP and VGAT/EGFP). Scale bars, 50 µm. (I) EGFP+ area in the PVN normalized to the number of EGFP+ nuclei in the Arc; $n = 3–4$ mice per group. (J) VGAT/EGFP co-localization in the PVH; $n = 3–4$ mice per group.

(K) Gene expression of *Crf* in the hypothalamus of AgRP-TRPV1 naive mice; $n = 5–6$ mice per group.

(L) Gene expression of *Crf* in the hypothalamus of C57BL/6J naive and EAE mice (7 dpi); $n = 5–6$ mice per group.

(legend continued on next page)

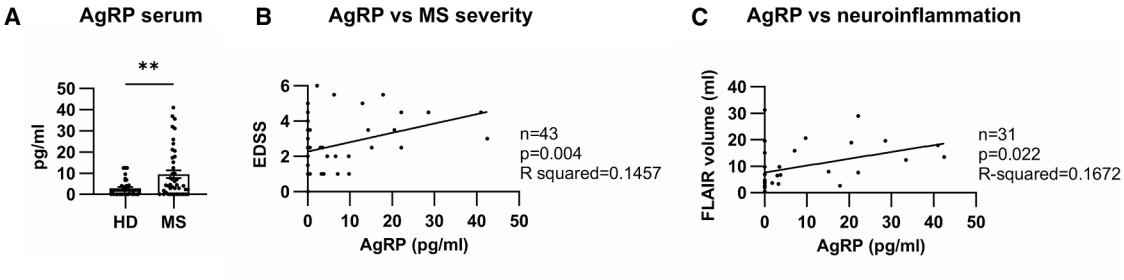

Figure 7. AgRP is increased in the serum of pwMS

(A) Concentration of AgRP peptide in the serum of 43 pwMS and 46 healthy donors (HDs).

(B) Linear regression analysis of AgRP concentration vs. EDSS in 43 pwMS.

(C) Linear regression analysis of AgRP concentration vs. FLAIR lesion volume in 31 pwMS.

Error bars are means ± sem. Data points indicate independent samples. $^{**}p < 0.01$ by Mann-Whitney *U* test (A) and R-square test (B and C).

We observed that chemogenetic activation of AgRP-cre neurons in AgRP-TRPV1 naive mice resulted in a reduction of *Crf* expression (Figure 6K). Instead, in EAE, the expression of *Crf* was increased (Figure 6L). This contrasting pattern suggests that, in the context of EAE, altered AgRP neuron signaling to the PVH may involve Crf-producing neurons.

The hypothalamus of EAE-induced mice exhibited signs of inflammation and astrocyte activation, as demonstrated by the increased expression of the proinflammatory cytokine interleukin-1 beta (*Il-1β*) and of glial fibrillary acidic protein (*Gfap*) at 7 and 15 dpi, which returned to basal levels at 25 dpi (Figures 6M and 6N). Altogether, these data indicate that inflammation occurs in the hypothalamus early in the pre-clinical phase of EAE, associated with altered electrical activity of AgRP neurons. Although the expression of *Agrp* in the hypothalamus also increased in both EAE and CFA mice at 7 dpi, it returned to basal levels at 15 dpi, while in EAE mice, the elevation persisted up to 15 dpi (Figure 6O). As the connection from peripheral organs to the brain is mediated through the vagal afferent pathway, we assessed whether the vagus nerve was involved in the increased expression of *Agrp* in the pre-clinical phase of EAE, by analyzing *Agrp* expression in the hypothalamus of mice subjected to unilateral cervical vagotomy and then immunized for EAE. In these mice, the increase of *Agrp* was significantly lower compared to that observed in sham-operated EAE-induced mice (Figure 6P), indicating that the vagus nerve is involved in the activation of AgRP neurons in the pre-clinical phase of EAE.

To understand whether the over-activation of AgRP neurons affected the course of EAE, we induced the disease in a DREADD model of chemogenetic inhibition of AgRP neurons, achieved by injecting AgRP-ires-cre mice with a cre-dependent AAV carrying the inhibitory hM4Di receptor and the mCherry reporter (AgRP-hM4Di mice[37]; Figure S13B). We observed a delay in disease onset and a reduction in severity in AgRP-hM4Di mice administered daily with CNO from the day of immunization compared to AgRP-hM4Di EAE mice administered with the vehicle (Figures 6Q–6S). In the BM, MPs and Neutro were reduced (Figures S13C and S13D), while Tregs in the thymus were increased (S13E). This was associated with reduced immune infiltration and demyelination in the spinal cord (Figures S13F–S13H). As previously reported in naive mice,[33] the inhibition of AgRP-cre neurons did not impact the body weight of immunized mice (Figure S13I). To rule out that the treatment effect on the disease was due to CNO administration itself, we verified that CNO had no effect on EAE when administered to wild-type C57Bl/6J mice (Figure S13J).

AgRP neuropeptide is increased in the serum of pwMS

To assess the potential involvement of AgRP neurons in MS, we measured levels of the AgRP peptide in the serum of 43 pwMS compared to 46 HD as a proxy of AgRP neuron activity.[38] Interestingly, the serum levels of AgRP were significantly increased in pwMS compared to HD (Figure 7A). Serum concentration of AgRP displayed a statistically significant correlation with higher scores on the Expanded Disability Status Scale (EDSS), a measure of disease severity (Figure 7B). Furthermore, in 31 pwMS who had undergone MRI at the time of blood sampling, we observed a direct correlation of AgRP levels with lesion volumes measured on fluid-attenuated inversion recovery (FLAIR) images, a measure of neuroinflammation (Figure 7C).

DISCUSSION

Integration of inflammatory signals takes place in different brain areas and leads to the modulation of the systemic immune response via different pathways, including the SNS[39] and

(M–P) C57BL/6 EAE mice, clinical scores (mean ± sem): 15 dpi (2.5 ± 0.52) and 25 dpi (2.06 ± 0.21). (M) Gene expression of *Il-1β* in the hypothalamus. Data are fold change vs. vehicle; *n* = 5–10 per group. (N) Gene expression of *Gfap* in the hypothalamus. Data are fold change vs. vehicle; *n* = 5–10 per group. (O) Gene expression of *Agrp* in the hypothalamus of CFA and EAE mice. Data are arbitrary units ($2^{-\Delta CT}$); *n* = 6–10 per group. (P) Gene expression of *Agrp* in the hypothalamus of sham-operated and vagotomized C57BL/6 EAE mice; *n* = 5 per group.

(Q–S) AgRP-hM4Di EAE mice. (Q) Kaplan-Meier analysis of disease onset; *n* = 10 mice per group. (R) Clinical course of EAE; *n* = 10 mice per group. (S) Quantification of the area under the curve (AUC) from 14 to 34 dpi; *n* = 10 mice per group. Error bars are mean ± sem. Data points indicate independent mice (A, C, and I–S) or brain slices (D–G).

$^{*}p < 0.05$, $^{**}p < 0.01$, $^{***}p < 0.001$, $^{****}p < 0.0001$; ns = not significant by Student's *t* test (A, I–L, and S), Mann-Whitney *U* test (D–G), one-way ANOVA/Tukey's test (M–O), and multiple unpaired Student's *t* test (P). See also Figures S11–S13.

AgRP neurons, which were recently reported to reduce peripheral inflammation.[40] Our study reveals that SNS signals target the hematopoietic niche upon induction of EAE, with increases in NE and TH-positive fibers within the BM. Additionally, genes negatively regulated by NE[4] displayed reduced expression, an effect that was reversed by severing nerve connections to the BM. An expansion of LSK cells, an early progenitor population of HSPCs, was observed from the pre-clinical phase of EAE. The rapid increase in the expression of proliferation and oxidative phosphorylation genes in BM stem cells reflects a stress-induced response to support heightened hematopoiesis.[41] We observed up-regulation of genes critical for stem cell proliferation, differentiation, and mobilization. These genes include *Stfa3*, known to promote HSPC expansion;[42] *Zic2*, an activator of the pluripotency and proliferation-linked octamer-binding protein 4 signaling pathway;[41,42] and *Prok2*, a potent driver of hematopoiesis.[43] These findings validate the augmentation of hematopoiesis in EAE. Interestingly, our data also demonstrated the up-regulation of genes associated with Th17 immune responses. This finding might be linked to the presence of autoreactive MOG-specific T cells in the BM, possibly driven by Ccr5 and Cxcl12, as reported by Shi et al.[27] However, while the RNAseq analysis confirmed the increased expression of *Ccr5* in the BM of EAE mice, we observed a significant reduction of *Cxcl12*, a major factor retaining HSPCs in the BM,[44] and of genes crucial for HSPC interaction with the BM stroma, such as *Tnc* and *Cald1*.[45,46] Our findings are in line with previous reports demonstrating that a decrease of *Cxcl12* within the BM following the release of NE[4,10] and, more recently, acetylcholine,[47] promotes hematopoiesis. Concomitant with the rise in NE and LSK cells, we observed an increased production of myeloid cells and an impaired generation of B lymphocytes, similar to what was reported by Shi and colleagues.[27] The reduction of *Cxcl12* in EAE may contribute to the increased mobilization of LSK cells and impaired B cell generation. Indeed, previous studies demonstrate an increased mobilization of HSPCs[44] and an impaired commitment of B lymphoid precursors in the BM[48] upon *Cxcl12* deletion. Our findings indicate that NE mediates the molecular and cellular changes observed in the BM of EAE mice through the activation of B3ARs, which are expressed by MSCs in the BM, as previously reported.[4] Blocking B3ARs reversed the effect of EAE on the expression of stem cell genes and mitigated the increase of Neutro and the reduction of B lymphocytes in the BM. These results are in line with previous studies demonstrating a role for B3ARs in hematopoiesis.[3–5,27,49] However, further analyses are needed to investigate the potential effects of the treatment on the functionality of Neutro and B lymphocytes, which determine their pro-inflammatory or regulatory role in the disease.[50,51] An increase in HSPCs has been demonstrated in the BM of pwMS.[27] In line with this finding, we observed a higher frequency of circulating $CD34^+$ cells in the BM of pwMS compared to HD.

Since the thymus lacks self-renewing hematopoietic cells, its T lymphocyte production relies on a constant influx of lymphoid progenitors migrating from the BM.[29,52] Our analysis of LSK cells in various compartments—the BM, blood, and the thymus—suggests that hematopoietic progenitors are released from the BM into the circulation and then increase in the thymus in EAE. Despite the surge of LSK precursors and mature single-positive CD4, CD8, and Treg lymphocytes, we observed a reduction in the number of thymus cells, mainly due to DP depletion. This observation is in line with previous works that report thymus atrophy in EAE and MS.[53–55] Reduction of DP precursor cells and alterations of chemokine production by TECs, including of *Cxcl12*, have been reported in response to infections.[56] Therefore, changes in cellular composition and gene expression in the thymus in EAE may reflect a general response to inflammation.

Our data demonstrated that the reduced expression of *Cxcl12* in the thymus of EAE mice is mediated by NE via B3ARs, which are expressed by TECs. Indeed, stimulation of B3ARs in naive mice led to decreased *Cxcl12* expression, mirroring the reduction observed in EAE in parallel with the NE increase. Moreover, inhibition of B3ARs in EAE prevented the reduction of *Cxcl12*. Cortical TECs are reported as the primary source of Cxcl12 in the thymus, while its receptor Cxcr4 is expressed only by immature thymocytes up to the DP stage.[14,57] The Cxcl12-Cxcr4 interaction helps retain maturing lymphocytes undergoing positive selection in the cortex; however, disrupting this interaction is not sufficient to allow DP precursors to leave the thymus cortex, as other molecules are involved.[14,57] In line with these observations, the inhibition of B3ARs in EAE was able to restore the expression of *Cxcl12* but not the frequency of DP precursors. Instead, the percentage of Cxcr4-expressing thymocytes increased, specifically among DN precursors, suggesting an increased chemoattraction of early precursors. Interestingly, the retention of maturing thymocytes within the cortex is essential for the process of positive selection,[57] a maturation step that has been proposed to be impaired in EAE.[58] Inhibition of B3ARs increased the frequency of Tregs not only in EAE but also in naive mice. Such an effect may be mediated by Il-15, a cytokine produced by mTECs and crucial for intra-thymic maturation of Tregs.[34,59] Indeed, we observed an increased expression of *Il-15* in the thymus upon inhibition of B3ARs. Collectively, our findings indicate that B3ARs play a role in the control of the thymic stromal microenvironment by the SNS.

Blocking B3ARs significantly delayed the onset and reduced the severity of EAE, indicating that activation of B3ARs contributed to disease development. The therapeutic effect of B3AR inhibition may be due to the reduction of myeloid hematopoiesis and the increase of Treg cell number and suppressive capacity, as suggested by the pathogenic role of CNS-invading myeloid cells[27,60] and the protective function of Treg.[61] In this direction, we observed a reduced presence of immune infiltrates in the CNS of EAE mice treated with the B3AR antagonist.

Our study not only unveils a role for the SNS in directing immune cell generation via B3ARs in EAE but also provides a proof of concept that hypothalamic AgRP neurons orchestrate the interplay between the SNS and B3ARs in the BM and thymus. Prior research has established a role for the hypothalamus in modulating adrenergic transmission within the BM. For instance, stimulation of the suprachiasmatic nucleus by light[4] and hypofunction of AgRP neurons[20] were demonstrated to raise NE levels in the BM. Our data reveal that the chemogenetic activation of AgRP-cre neurons leads to decreased NE levels in both BM and thymus. This was associated with diminished c-FOS

expression in the PVH, a major hypothalamic nucleus regulating SNS activity. Our data are in line with previous works demonstrating that AgRP neurons inhibit neurons in the PVH[62] and reduce the firing rate of sympathetic nerves.[17,23] The reduction of NE in the BM upon chemogenetic activation of AgRP-cre neurons increased *Cxcl12* expression and reduced the frequency of MP and neutrophils in the BM. Our findings are consistent with the recent discovery of hypothalamus-BM connections that control hematopoiesis[63] and drive the immune response to physical threats through shaping leukocyte repertoire.[64] We observed a reduction of NE upon chemogenetic activation of AgRP-cre neurons also in the thymus, which was associated with an increase in *Cxcl12* and *Il-15* expression and in the frequency of Tregs. These findings support the role of AgRP neurons in the neural control of thymic stromal cells and Tregs. Notably, previous research demonstrated an impaired ability of the thymus to produce Tregs in AgRP Sirt1$^{-/-}$ EAE mice, which are characterized by hypofunctional AgRP neurons.[21] This observation, coupled with our finding that the chemogenetic activation of AgRP-cre neurons induces *Il-15* expression in the thymus, suggests that the intra-thymic increase of Treg may be due to *de novo* production.

Mechanistically, the stimulation of AgRP-cre neurons inhibits B3ARs in the BM and thymus, expanding previous reports obtained in the adipose tissue.[23] Indeed, chemogenetic activation of AgRP-cre neurons mimics the effects of B3AR blockade, and administration of a B3AR agonist abolishes these effects. Chemogenetic activation of AgRP neurons increased Treg in the thymus and reduced myeloid cells in the BM, suggesting a possible immune-regulatory effect, further supported by a recent study demonstrating that chemogenetic activation of AgRP-cre neurons reduces inflammation via their projection to the PVH[40] and results in fewer inflammatory monocytes in the circulation.[65]

Our study revealed that the effects of AgRP neuron activation induced by chemogenetic stimulation in naive mice differ from those observed in EAE, in which AgRP neurons display signs of increased activation. While chemogenetic activation of AgRP-cre neurons in naive mice resulted in decreased BM and thymus NE levels, EAE was associated with high baseline NE levels that could not be reduced by chemogenetic stimulation. Moreover, chemogenetic activation of AgRP-cre neurons in naive mice reduced c-Fos in the PVH, while this was not observed in EAE mice. The different extent of the chemogenetic and disease-mediated activation of AgRP neurons is likely the consequence of a dysfunctional connection between AgRP neurons and the PVH, leading to an impaired inhibitory control of the PVH by AgRP neurons in the context of EAE. Indeed, we observed a significant loss of inhibitory AgRP synapses in the PVH during the pre-clinical phase of the disease. Moreover, the expression of *Crf* in the hypothalamus, a neuropeptide produced in the PVH,[35] was reduced following the chemogenetic activation of AgRP-cre neurons in naive mice but was increased in EAE, further suggesting altered AgRP-to-PVH connectivity. Interestingly, synapse engulfment and loss in diverse brain regions have been previously documented in early EAE stages, occurring independently of demyelination and linked to microglia activation.[66,67] Microglia-mediated synapse elimination processes have also been described in mouse models of neurodegenerative diseases[68–71] suggesting that activated microglia may be involved in the loss of AgRP synapses in the PVH during EAE. Alternatively, we could also speculate that while acute activation of AgRP-cre neurons induced by chemogenetic tools in naive mice increases their physiological inhibitory action on the PVH, the chronic activation of AgRP neurons observed in EAE could activate more complex mechanisms, possibly implying plastic changes of the circuit and causing rewiring of the areas involved, including a loss of axonal fibers. It is known that pathological chronic increased firing frequency can cause, for instance, excessive calcium influx and impairments of axonal transport, which eventually contribute to axonal degeneration.[72,73]

Importantly, we observed that the chemogenetic inhibition of AgRP neurons during EAE ameliorated the clinical course and reduced susceptibility to the disease, confirming that AgRP neurons are relevant for the disease.[21]

We also demonstrated that, upon unilateral vagotomy in EAE mice, *Agrp* expression was significantly diminished compared to sham-operated EAE mice. This suggests that vagal sensory fibers from the periphery are required for the activation of AgRP neurons in EAE. Previous studies demonstrated that AgRP neurons express cytokine receptors and can sense both systemic and brain administration of IL-1β[74] and IL-17,[75] two well-known CNS inflammation-associated cytokines. Thus, inflammatory cues may also participate in the activation of AgRP neurons in EAE. The activation of AgRP neurons in the pre-clinical phase of EAE is likely elicited by signals not related to brain damage, as indicated by the increased *Agrp* expression observed at this stage in mice sham-immunized with CFA, which did not develop CNS pathology. We observed an increase in the expression of *Gfap*, a marker of astrocyte activation, and of the pro-inflammatory cytokine *Il-1β* in the pre-clinical and acute phases of EAE, mirroring the augmented expression of *Agrp*. Interestingly, stimulation of AgRP neurons has been shown to induce astrocyte activation, potentially creating a positive feedback loop in which astrocytes sustain AgRP neuron activity.[76] Whether AgRP neuron dysfunction is the cause or the consequence of hypothalamic inflammation remains to be established. Our study did not directly investigate the involvement of myelin-specific T cells in the observed alterations of AgRP neurons in EAE. However, the finding that *Agrp* expression was also increased as an early response to immunization with CFA, in mice that do not develop autoreactive T cells, suggests that these cells are not involved in this process.

To provide a translational value to our study, we assessed the possible role of the AgRP neuropeptide as a biomarker in pwMS. Indeed, AgRP neuropeptide is elevated in the serum of pwMS, and its levels correlated with both disease severity (measured by EDSS) and the presence of FLAIR lesions, a marker of brain inflammation.[77] Although little attention has been paid to clinical functions controlled by the hypothalamus in MS[78] hypothalamic autoptic lesions and MRI abnormalities,[79,80] as well as increased activity of the hypothalamic-pituitary-adrenal (HPA) axis,[81] have been reported. Further studies are needed to clarify the significance of increased AgRP peptide in the context of MS pathogenesis and to assess its potential clinical relevance as a biomarker of hypothalamic dysfunction.

In conclusion, our study reveals that AgRP neurons regulate hematopoiesis by reducing NE in the BM and thymus, thereby

attenuating the activation of B3ARs. The relevance of this finding is emphasized by our discovery that NE and B3ARs are involved in the pathogenesis of EAE and by the observation that AgRP neurons are dysfunctional in EAE and, possibly, in MS.

Limitations of the study

Although we have shown that B3ARs mediate the effect of chemogenetic activation of AgRP neurons on hematopoiesis and intrathymic frequency of Treg, the precise molecular mechanisms underlying these processes remain to be elucidated. Moreover, *in vivo* electrophysiological recordings at the single-cell level will be required to properly confirm that, in EAE, the recorded neuronal hyperactivity of the Arc originates from AgRP neurons. Additionally, the specific role of AgRP neuron activation in neuroinflammation, both in animal models and humans, necessitates additional investigation, including identification of the upstream signals triggering AgRP neuron activation in EAE and MS. Finally, despite our observation of elevated AgRP peptide levels in the serum of pwMS, more studies on larger cohorts are essential to determine the clinical significance of this finding and its potential implications.

RESOURCE AVAILABILITY

Lead contact

Further information and requests for resources and reagents should be directed to and will be fulfilled by the lead contact, Tiziana Vigo (tiziana.vigo@hsanmartino.it).

Materials availability

Materials generated in the study will be available upon request to the lead contact.

Data and code availability

All data are available in the main text or in the supplemental information or in method details. Sequencing data have been deposited to GEO database under the reference series GEO: GSE214765. Raw sequencing data have been deposited at the NCBI Sequence Read Archive (SRA) under accession number SRP400969 and associated with BioProject PRJNA887047. Any additional information required to reanalyze the data reported in this paper is available from the lead contact upon request.

ACKNOWLEDGMENTS

This work was funded by European Union - Next Generation EU - NRRP M6C2 - Investment 2.1 Enhancement and strengthening of biomedical research in the NHS (project PNRR-MAD-2022-12376126, CUP C13C22000970006 to A.U.). This work was in part supported by Fondazione Italiana Sclerosi Multipla (grant 2019/R-single_038 to A.U.; grant 2017/R/28 to T.V.; grant 2018/R/7 to A.L.; grant 2018/S/5 to G.M.; grant 2022-PR-Single/013 to C.P., and grant 2023/R-Single/047 to G.G.); Compagnia di San Paolo (ROL 32617 to A.U. and ROL 34760 to F.B.); Italian Ministry of Health (GR-2016-02361163 to A.L. and GR-2019-12370176 to G.G.); Italian Ministry for Education, University and Research (grant 2017K55HLC to A.L. and G.M. and REPAIR FIS_00002258 to M.I.); ERACOSYSMED ERA-Net program and Italian Ministry of Health (PER-2012-2361136 - Personalizing health care in Multiple Sclerosis using system medicine tools [Sys4MS] to A.U.); #NEXTGENERATIONEU (NGEU) and funded by the Ministry of University and Research (MUR), National Recovery and Resilience Plan (NRRP), project MNESYS (PE0000006) – (DN. 1553 11.10.2022 to A.U., T.V., A.L., and G.M.); Italian Ministry of Health, Next Generation (EU, M6/C2_CALL 2022 cod. PNRR-MAD-2022-12375634 to G.M.); Italian Ministry of Health, National Recovery and Resilience Plan (PNRR), Next Generation (EU, M6/C2_CALL 2023, cod PNRR-MCNT2-2023-12378040 to G.M.); and National Recovery and Resilience Plan (NRRP), Mission 4, Component 2 (M4C2), Investment 1.1, by the Italian Ministry of University and Research (MUR), funded by NextGenerationEU (call for tender no. 1409 - P2022T4PKT-CUP B53D23024820001 to C.P. and call for tender no. 104 -2022LNHZAP – CUP E53D23013240006 to G.M.). We thank the Nikon Imaging Center at the IIT for help with microscopy. We also thank Dr. Francesco Papaleo and Dr. Lucilla Nobbio for help with histological analysis and Dr. Irene Cossu for technical and administrative support.

AUTHOR CONTRIBUTIONS

Conceptualization, T.V., N.K.d.R., and A.U.; methodology, M.C.M., E.R., G.Z., G.G., E. Cornacchia, A.P., T.A., G. Capodivento, G.F., C.B., S.S.S., S.F., L.L., M.S., C.P., L.F., E. Cerutti, A.L., J.C., and M.I.; investigation, M.C.M., E.R., G.Z., G.G., E. Cornacchia, A.P., T.A., G. Cirmena, G.F., C.B., S.S.S., S.F., L.L., M.S., C.P., D.C., L.F., E. Cerutti, A.L., G.M., J.C., A.P., C.R., G. Capodivento, M.B., and M.I.; writing – original draft, T.V., A.U., and T.L.H.; visualization, M.C.M., E.R., G.Z., G.G., E. Cornacchia, A.P., T.A., G. Capodivento, G.F., C.B., S.S.S., S.F., L.L., M.S., C.P., D.C., L.F., E. Cerutti, and J.C.; writing – review & editing, all co-authors; funding acquisition, T.V., A.L., G.M., A.U., F.B., G.G., M.I., and C.P.; and supervision, N.K.d.R., T.L.H., F.B., and A.U.

DECLARATION OF INTERESTS

The authors declare no competing interests.

STAR★METHODS

Detailed methods are provided in the online version of this paper and include the following:

- KEY RESOURCES TABLE
- EXPERIMENTAL MODEL AND STUDY PARTICIPANT DETAILS
  - Mice
  - Human subjects
- METHOD DETAILS
  - Study design
  - EAE and treatments
  - Neuropathology analysis of EAE
  - Viral injection
  - Surgery
  - NE quantification
  - Flow cytometry
  - Confocal and fluorescence microscopy
  - Real-Time PCR
  - *In vivo* extracellular recordings
  - RNA sequencing
  - AgRP neuropeptide quantification
  - Brain MRI
- QUANTIFICATION AND STATISTICAL ANALYSIS

SUPPLEMENTAL INFORMATION

Supplemental information can be found online at https://doi.org/10.1016/j.celrep.2025.116556.

Received: February 26, 2025
Revised: June 8, 2025
Accepted: October 23, 2025

REFERENCES

1. Lucas, D., Bruns, I., Battista, M., Mendez-Ferrer, S., Magnon, C., Kunisaki, Y., and Frenette, P.S. (2012). Norepinephrine reuptake inhibition promotes mobilization in mice: potential impact to rescue low stem

cell yields. Blood *119*, 3962–3965. https://doi.org/10.1182/blood-2011-07-367102.

2. Méndez-Ferrer, S., Battista, M., and Frenette, P.S. (2010). Cooperation of beta(2)- and beta(3)-adrenergic receptors in hematopoietic progenitor cell mobilization. Ann. N. Y. Acad. Sci. *1192*, 139–144. https://doi.org/10.1111/j.1749-6632.2010.05390.x.

3. Ho, Y.-H., Del Toro, R., Rivera-Torres, J., Rak, J., Korn, C., García-García, A., Macías, D., González-Gómez, C., Del Monte, A., Wittner, M., et al. (2019). Remodeling of Bone Marrow Hematopoietic Stem Cell Niches Promotes Myeloid Cell Expansion during Premature or Physiological. Cell Stem Cell *25*, 407–418.e6. https://doi.org/10.1016/j.stem.2019.06.007.

4. Méndez-Ferrer, S., Michurina, T.V., Ferraro, F., Mazloom, A.R., Macarthur, B.D., Lira, S.A., Scadden, D.T., Ma'ayan, A., Enikolopov, G.N., and Frenette, P.S. (2010). Mesenchymal and haematopoietic stem cells form a unique bone marrow niche. Nature *466*, 829–834. https://doi.org/10.1038/nature09262.

5. Maryanovich, M., Zahalka, A.H., Pierce, H., Pinho, S., Nakahara, F., Asada, N., Wei, Q., Wang, X., Ciero, P., Xu, J., et al. (2018). Adrenergic nerve degeneration in bone marrow drives aging of the hematopoietic stem cell niche. Nat. Med. *24*, 782–791. https://doi.org/10.1038/s41591-018-0030-x.

6. Ferraro, F., Lymperi, S., Méndez-Ferrer, S., Saez, B., Spencer, J.A., Yeap, B.Y., Masselli, E., Graiani, G., Prezioso, L., Rizzini, E.L., et al. (2011). Diabetes impairs hematopoietic stem cell mobilization by altering niche function. Sci. Transl. Med. *3*, 104ra101. https://doi.org/10.1126/scitranslmed.3002191.

7. Arranz, L., Sánchez-Aguilera, A., Martín-Pérez, D., Isern, J., Langa, X., Tzankov, A., Lundberg, P., Muntión, S., Tzeng, Y.-S., Lai, D.-M., et al. (2014). Neuropathy of haematopoietic stem cell niche is essential for myeloproliferative neoplasms. Nature *512*, 78–81. https://doi.org/10.1038/nature13383.

8. Shi, S.X., Shi, K., and Liu, Q. (2021). Brain injury instructs bone marrow cellular lineage destination to reduce neuroinflammation. Sci. Transl. Med. *13*, eabc7029. https://doi.org/10.1126/scitranslmed.abc7029.

9. Courties, G., Herisson, F., Sager, H.B., Heidt, T., Ye, Y., Wei, Y., Sun, Y., Severe, N., Dutta, P., Scharff, J., et al. (2015). Ischemic stroke activates hematopoietic bone marrow stem cells. Circ. Res. *116*, 407–417. https://doi.org/10.1161/CIRCRESAHA.116.305207.

10. Heidt, T., Sager, H.B., Courties, G., Dutta, P., Iwamoto, Y., Zaltsman, A., von Zur Muhlen, C., Bode, C., Fricchione, G.L., Denninger, J., et al. (2014). Chronic variable stress activates hematopoietic stem cells. Nat. Med. *20*, 754–758. https://doi.org/10.1038/nm.3589.

11. Kfoury, Y., and Scadden, D.T. (2015). Mesenchymal cell contributions to the stem cell niche. Cell Stem Cell *16*, 239–253. https://doi.org/10.1016/j.stem.2015.02.019.

12. Lind, E.F., Prockop, S.E., Porritt, H.E., and Petrie, H.T. (2001). Mapping precursor movement through the postnatal thymus reveals specific microenvironments supporting defined stages of early lymphoid development. J. Exp. Med. *194*, 127–134. https://doi.org/10.1084/jem.194.2.127.

13. Leposavić, G., Pilipović, I., and Perišić, M. (2011). Cellular and nerve fibre catecholaminergic thymic network: steroid hormone dependent activity. Physiol. Res. *60*, S71–S82. https://doi.org/10.33549/physiolres.932175.

14. Lucas, B., White, A.J., Parnell, S.M., Henley, P.M., Jenkinson, W.E., and Anderson, G. (2017). Progressive Changes in CXCR4 Expression That Define Thymocyte Positive Selection Are Dispensable For Both Innate and Conventional αβT-cell Development. Sci. Rep. *7*, 5068. https://doi.org/10.1038/s41598-017-05182-7.

15. Trotter, R.N., Stornetta, R.L., Guyenet, P.G., and Roberts, M.R. (2007). Transneuronal mapping of the CNS network controlling sympathetic outflow to the rat thymus. Auton. Neurosci. *131*, 9–20. https://doi.org/10.1016/j.autneu.2006.06.001.

16. Ryu, V., Gumerova, A.A., Witztum, R., Korkmaz, F., Cullen, L., Kannangara, H., Moldavski, O., Barak, O., Lizneva, D., Goosens, K.A., et al. (2024). An atlas of brain-bone sympathetic neural circuits in mice. eLife *13*, e95727. https://doi.org/10.7554/eLife.95727.

17. Shi, Z., Madden, C.J., and Brooks, V.L. (2017). Arcuate neuropeptide Y inhibits sympathetic nerve activity via multiple neuropathways. J. Clin. Investig. *127*, 2868–2880. https://doi.org/10.1172/JCI92008.

18. Gropp, E., Shanabrough, M., Borok, E., Xu, A.W., Janoschek, R., Buch, T., Plum, L., Balthasar, N., Hampel, B., Waisman, A., et al. (2005). Agouti-related peptide-expressing neurons are mandatory for feeding. Nat. Neurosci. *8*, 1289–1291. https://doi.org/10.1038/nn1548.

19. Dietrich, M.O., Antunes, C., Geliang, G., Liu, Z.-W., Borok, E., Nie, Y., Xu, A.W., Souza, D.O., Gao, Q., Diano, S., et al. (2010). Agrp neurons mediate Sirt1's action on the melanocortin system and energy balance: roles for Sirt1 in neuronal firing and synaptic plasticity. J. Neurosci. *30*, 11815–11825. https://doi.org/10.1523/JNEUROSCI.2234-10.2010.

20. Kim, J.G., Sun, B.-H., Dietrich, M.O., Koch, M., Yao, G.-Q., Diano, S., Insogna, K., and Horvath, T.L. (2015). AgRP Neurons Regulate Bone Mass. Cell Rep. *13*, 8–14. https://doi.org/10.1016/j.celrep.2015.08.070.

21. Matarese, G., Procaccini, C., Menale, C., Kim, J.G., Kim, J.D., Diano, S., Diano, N., De Rosa, V., Dietrich, M.O., and Horvath, T.L. (2013). Hunger-promoting hypothalamic neurons modulate effector and regulatory T-cell responses. Proc. Natl. Acad. Sci. USA *110*, 6193–6198. https://doi.org/10.1073/pnas.1210644110.

22. Dietrich, M.O., Zimmer, M.R., Bober, J., and Horvath, T.L. (2015). Hypothalamic Agrp neurons drive stereotypic behaviors beyond feeding. Cell *160*, 1222–1232. https://doi.org/10.1016/j.cell.2015.02.024.

23. Cavalcanti-de-Albuquerque, J.P., Bober, J., Zimmer, M.R., and Dietrich, M.O. (2019). Regulation of substrate utilization and adiposity by Agrp neurons. Nat. Commun. *10*, 311. https://doi.org/10.1038/s41467-018-08239-x.

24. Pearce, E.L., and Pearce, E.J. (2013). Metabolic pathways in immune cell activation and quiescence. Immunity *38*, 633–643. https://doi.org/10.1016/j.immuni.2013.04.005.

25. Lee, A.H., and Dixit, V.D. (2020). Dietary Regulation of Immunity. Immunity *53*, 510–523. https://doi.org/10.1016/j.immuni.2020.08.013.

26. Suda, T., Takubo, K., and Semenza, G.L. (2011). Metabolic regulation of hematopoietic stem cells in the hypoxic niche. Cell Stem Cell *9*, 298–310. https://doi.org/10.1016/j.stem.2011.09.010.

27. Shi, K., Li, H., Chang, T., He, W., Kong, Y., Qi, C., Li, R., Huang, H., Zhu, Z., Zheng, P., et al. (2022). Bone marrow hematopoiesis drives multiple sclerosis progression. Cell *185*, 2234–2247.e17. https://doi.org/10.1016/j.cell.2022.05.020.

28. Doronin, V.B., Parkhomenko, T.A., Korablev, A., Toporkova, L.B., Lopatnikova, J.A., Alshevskaja, A.A., Sennikov, S.V., Buneva, V.N., Budde, T., Meuth, S.G., et al. (2016). Changes in different parameters, lymphocyte proliferation and hematopoietic progenitor colony formation in EAE mice treated with myelin oligodendrocyte glycoprotein. J. Cell Mol. Med. *20*, 81–94. https://doi.org/10.1111/jcmm.12704.

29. Lai, A.Y., and Kondo, M. (2007). Identification of a bone marrow precursor of the earliest thymocytes in adult mouse. Proc. Natl. Acad. Sci. USA *104*, 6311–6316. https://doi.org/10.1073/pnas.0609608104.

30. Atasoy, D., Betley, J.N., Su, H.H., and Sternson, S.M. (2012). Deconstruction of a neural circuit for hunger. Nature *488*, 172–177. https://doi.org/10.1038/nature11270.

31. Betley, J.N., Cao, Z.F.H., Ritola, K.D., and Sternson, S.M. (2013). Parallel, redundant circuit organization for homeostatic control of feeding behavior. Cell *155*, 1337–1350. https://doi.org/10.1016/j.cell.2013.11.002.

32. Krashes, M.J., Koda, S., Ye, C., Rogan, S.C., Adams, A.C., Cusher, D.S., Maratos-Flier, E., Roth, B.L., and Lowell, B.B. (2011). Rapid, reversible activation of AgRP neurons drives feeding behavior in mice. J. Clin. Investig. *121*, 1424–1428. https://doi.org/10.1172/JCI46229.

33. Decourt, C., Connolly, G.A.D.P., Ancel, C., Inglis, M.A., and Anderson, G.M. (2022). Agouti-related peptide neuronal silencing overcomes delayed puberty in neonatally underfed male mice. J. Neuroendocrinol. *34*, e13190. https://doi.org/10.1111/jne.13190.

34. Cui, G., Hara, T., Simmons, S., Wagatsuma, K., Abe, A., Miyachi, H., Kitano, S., Ishii, M., Tani-ichi, S., and Ikuta, K. (2014). Characterization of the IL-15 niche in primary and secondary lymphoid organs in vivo. Proc. Natl. Acad. Sci. USA *111*, 1915–1920. https://doi.org/10.1073/pnas.1318281111.

35. Rajamanickam, S., and Justice, N.J. (2022). Hypothalamic corticotropin-releasing factor neurons modulate behavior, endocrine, and autonomic stress responses via direct synaptic projections. Current Opinion in Endocrine and Metabolic Research *26*, 100400. https://doi.org/10.1016/j.coemr.2022.100400.

36. Udelsman, R., Harwood, J.P., Millan, M.A., Chrousos, G.P., Goldstein, D.S., Zimlichman, R., Catt, K.J., and Aguilera, G. (1986). Functional corticotropin releasing factor receptors in the primate peripheral sympathetic nervous system. Nature *319*, 147–150. https://doi.org/10.1038/319147a0.

37. Chen, W., Mehlkop, O., Scharn, A., Nolte, H., Klemm, P., Henschke, S., Steuernagel, L., Sotelo-Hitschfeld, T., Kaya, E., Wunderlich, C.M., et al. (2023). Nutrient-sensing AgRP neurons relay control of liver autophagy during energy deprivation. Cell Metab. *35*, 786–806.e13. https://doi.org/10.1016/j.cmet.2023.03.019.

38. Shen, C.-P., Wu, K.K., Shearman, L.P., Camacho, R., Tota, M.R., Fong, T.M., and Van der Ploeg, L.H.T. (2002). Plasma agouti-related protein level: a possible correlation with fasted and fed states in humans and rats. J. Neuroendocrinol. *14*, 607–610. https://doi.org/10.1046/j.1365-2826.2002.00825.x.

39. Pavlov, V.A., and Tracey, K.J. (2017). Neural regulation of immunity: molecular mechanisms and clinical translation. Nat. Neurosci. *20*, 156–166. https://doi.org/10.1038/nn.4477.

40. Klima, M.L., Kruger, K.A., Goldstein, N., Pulido, S., Low, A.Y.T., Assenmacher, C.-A., Alhadeff, A.L., and Betley, J.N. (2023). Anti-inflammatory effects of hunger are transmitted to the periphery via projection-specific AgRP circuits. Cell Rep. *42*, 113338. https://doi.org/10.1016/j.celrep.2023.113338.

41. Lagadinou, E.D., Sach, A., Callahan, K., Rossi, R.M., Neering, S.J., Minhajuddin, M., Ashton, J.M., Pei, S., Grose, V., O'Dwyer, K.M., et al. (2013). BCL-2 inhibition targets oxidative phosphorylation and selectively eradicates quiescent human leukemia stem cells. Cell Stem Cell *12*, 329–341. https://doi.org/10.1016/j.stem.2012.12.013.

42. Bilodeau, M., MacRae, T., Gaboury, L., Laverdure, J.-P., Hardy, M.-P., Mayotte, N., Paradis, V., Harton, S., Perreault, C., and Sauvageau, G. (2009). Analysis of Blood Stem Cell Activity and Cystatin Gene Expression in a Mouse Model Presenting a Chromosomal Deletion Encompassing Csta and Stfa2l1. PLoS One *4*, e7500. https://doi.org/10.1371/journal.pone.0007500.

43. Ngan, E.S.W., and Tam, P.K.H. (2008). Prokineticin-signaling pathway. Int. J. Biochem. Cell Biol. *40*, 1679–1684. https://doi.org/10.1016/j.biocel.2008.03.010.

44. Petit, I., Szyper-Kravitz, M., Nagler, A., Lahav, M., Peled, A., Habler, L., Ponomaryov, T., Taichman, R.S., Arenzana-Seisdedos, F., Fujii, N., et al. (2002). G-CSF induces stem cell mobilization by decreasing bone marrow SDF-1 and up-regulating CXCR4. Nat. Immunol. *3*, 687–694. https://doi.org/10.1038/ni813.

45. Chiquet-Ehrismann, R., Orend, G., Chiquet, M., Tucker, R.P., and Midwood, K.S. (2014). Tenascins in stem cell niches. Matrix Biol. *37*, 112–123. https://doi.org/10.1016/j.matbio.2014.01.007.

46. Wagner, W., Wein, F., Roderburg, C., Saffrich, R., Faber, A., Krause, U., Schubert, M., Benes, V., Eckstein, V., Maul, H., and Ho, A.D. (2007). Adhesion of hematopoietic progenitor cells to human mesenchymal stem cells as a model for cell-cell interaction. Exp. Hematol. *35*, 314–325. https://doi.org/10.1016/j.exphem.2006.10.003.

47. Schloss, M.J., Hulsmans, M., Rohde, D., Lee, I.-H., Severe, N., Foy, B.H., Pulous, F.E., Zhang, S., Kokkaliaris, K.D., Frodermann, V., et al. (2022). B lymphocyte-derived acetylcholine limits steady-state and emergency hematopoiesis. Nat. Immunol. *23*, 605–618. https://doi.org/10.1038/s41590-022-01165-7.

48. Greenbaum, A., Hsu, Y.-M.S., Day, R.B., Schuettpelz, L.G., Christopher, M.J., Borgerding, J.N., Nagasawa, T., and Link, D.C. (2013). CXCL12 in early mesenchymal progenitors is required for haematopoietic stem-cell maintenance. Nature *495*, 227–230. https://doi.org/10.1038/nature11926.

49. Zhang, Z., Huang, Z., Ong, B., Sahu, C., Zeng, H., and Ruan, H.-B. (2019). Bone marrow adipose tissue-derived stem cell factor mediates metabolic regulation of hematopoiesis. Haematologica *104*, 1731–1743. https://doi.org/10.3324/haematol.2018.205856.

50. Rumble, J.M., Huber, A.K., Krishnamoorthy, G., Srinivasan, A., Giles, D.A., Zhang, X., Wang, L., and Segal, B.M. (2015). Neutrophil-related factors as biomarkers in EAE and MS. J. Exp. Med. *212*, 23–35. https://doi.org/10.1084/jem.20141015.

51. Allan, S. (2008). Balancing B-cell subsets in EAE. Nat. Rev. Immunol. *8*, 825. https://doi.org/10.1038/nri2439.

52. Yu, V.W.C., Saez, B., Cook, C., Lotinun, S., Pardo-Saganta, A., Wang, Y.-H., Lymperi, S., Ferraro, F., Raaijmakers, M.H.G.P., Wu, J.Y., et al. (2015). Specific bone cells produce DLL4 to generate thymus-seeding progenitors from bone marrow. J. Exp. Med. *212*, 759–774. https://doi.org/10.1084/jem.20141843.

53. Dg, H., Jd, H., D, D., L, F.-G., E, Z., H, M., Y, L., J, A., and A, B.-O. (2011). Reduced thymic output and peripheral naïve CD4 T-cell alterations in primary progressive multiple sclerosis (PPMS). J. Neuroimmunol. *233*, 233–239. https://doi.org/10.1016/j.jneuroim.2010.12.007.

54. Duszczyszyn, D.A., Williams, J.L., Mason, H., Lapierre, Y., Antel, J., and Haegert, D.G. (2010). Thymic involution and proliferative T-cell responses in multiple sclerosis. J. Neuroimmunol. *221*, 73–80. https://doi.org/10.1016/j.jneuroim.2010.02.005.

55. das Neves, S.P., Serre-Miranda, C., Nobrega, C., Roque, S., Cerqueira, J.J., Correia-Neves, M., and Marques, F. (2018). Immune Thymic Profile of the MOG-Induced Experimental Autoimmune Encephalomyelitis Mouse Model. Front. Immunol. *9*, 2335. https://doi.org/10.3389/fimmu.2018.02335.

56. Savino, W. (2006). The thymus is a common target organ in infectious diseases. PLoS Pathog. *2*, e62. https://doi.org/10.1371/journal.ppat.0020062.

57. Kadakia, T., Tai, X., Kruhlak, M., Wisniewski, J., Hwang, I.-Y., Roy, S., Guinter, T.I., Alag, A., Kehrl, J.H., Zhuang, Y., and Singer, A. (2019). E-protein-regulated expression of CXCR4 adheres preselection thymocytes to the thymic cortex. J. Exp. Med. *216*, 1749–1761. https://doi.org/10.1084/jem.20182285.

58. Jiang, Q., Ma, X., Zhu, G., Si, W., He, L., and Yang, G. (2024). Altered T cell development in an animal model of multiple sclerosis. Exp. Neurol. *371*, 114579. https://doi.org/10.1016/j.expneurol.2023.114579.

59. Apert, C., Romagnoli, P., and van Meerwijk, J.P.M. (2018). IL-2 and IL-15 dependent thymic development of Foxp3-expressing regulatory T lymphocytes. Protein Cell *9*, 322–332. https://doi.org/10.1007/s13238-017-0425-3.

60. Gullotta, G.S., De Feo, D., Friebel, E., Semerano, A., Scotti, G.M., Bergamaschi, A., Butti, E., Brambilla, E., Genchi, A., Capotondo, A., et al. (2023). Age-induced alterations of granulopoiesis generate atypical neutrophils that aggravate stroke pathology. Nat. Immunol. *24*, 925–940. https://doi.org/10.1038/s41590-023-01505-1.

61. Koutrolos, M., Berer, K., Kawakami, N., Wekerle, H., and Krishnamoorthy, G. (2014). Treg cells mediate recovery from EAE by controlling effector T cell proliferation and motility in the CNS. Acta Neuropathol. Commun. *2*, 163. https://doi.org/10.1186/s40478-014-0163-1.

62. Ghamari-Langroudi, M., Digby, G.J., Sebag, J.A., Millhauser, G.L., Palomino, R., Matthews, R., Gillyard, T., Panaro, B.L., Tough, I.R., Cox,

H.M., et al. (2015). G-protein-independent coupling of MC4R to Kir7.1 in hypothalamic neurons. Nature *520*, 94–98. https://doi.org/10.1038/nature14051.

63. McAlpine, C.S., Kiss, M.G., Rattik, S., He, S., Vassalli, A., Valet, C., Anzai, A., Chan, C.T., Mindur, J.E., Kahles, F., et al. (2019). Sleep modulates haematopoiesis and protects against atherosclerosis. Nature *566*, 383–387. https://doi.org/10.1038/s41586-019-0948-2.

64. Poller, W.C., Downey, J., Mooslechner, A.A., Khan, N., Li, L., Chan, C.T., McAlpine, C.S., Xu, C., Kahles, F., He, S., et al. (2022). Brain motor and fear circuits regulate leukocytes during acute stress. Nature *607*, 578–584. https://doi.org/10.1038/s41586-022-04890-z.

65. Cavalcanti De Albuquerque, J.P., Hunter, J., Domingues, R.G., Harno, E., Worth, A.A., Liguori, F.M., D'Alessio, A., Aviello, G., Bechtold, D., White, A., et al. (2025). Brain sensing of metabolic state regulates circulating monocytes. Sci. Immunol. *10*, eadr3226. https://doi.org/10.1126/sciimmunol.adr3226.

66. Centonze, D., Muzio, L., Rossi, S., Cavasinni, F., De Chiara, V., Bergami, A., Musella, A., D'Amelio, M., Cavallucci, V., Martorana, A., et al. (2009). Inflammation triggers synaptic alteration and degeneration in experimental autoimmune encephalomyelitis. J. Neurosci. *29*, 3442–3452. https://doi.org/10.1523/JNEUROSCI.5804-08.2009.

67. Werneburg, S., Jung, J., Kunjamma, R.B., Ha, S.-K., Luciano, N.J., Willis, C.M., Gao, G., Biscola, N.P., Havton, L.A., Crocker, S.J., et al. (2020). Targeted Complement Inhibition at Synapses Prevents Microglial Synaptic Engulfment and Synapse Loss in Demyelinating Disease. Immunity *52*, 167–182.e7. https://doi.org/10.1016/j.immuni.2019.12.004.

68. Hong, S., Beja-Glasser, V.F., Nfonoyim, B.M., Frouin, A., Li, S., Ramakrishnan, S., Merry, K.M., Shi, Q., Rosenthal, A., Barres, B.A., et al. (2016). Complement and microglia mediate early synapse loss in Alzheimer mouse models. Science *352*, 712–716. https://doi.org/10.1126/science.aad8373.

69. Lui, H., Zhang, J., Makinson, S.R., Cahill, M.K., Kelley, K.W., Huang, H.-Y., Shang, Y., Oldham, M.C., Martens, L.H., Gao, F., et al. (2016). Progranulin Deficiency Promotes Circuit-Specific Synaptic Pruning by Microglia via Complement Activation. Cell *165*, 921–935. https://doi.org/10.1016/j.cell.2016.04.001.

70. Paolicelli, R.C., Jawaid, A., Henstridge, C.M., Valeri, A., Merlini, M., Robinson, J.L., Lee, E.B., Rose, J., Appel, S., Lee, V.M.-Y., et al. (2017). TDP-43 Depletion in Microglia Promotes Amyloid Clearance but Also Induces Synapse Loss. Neuron *95*, 297–308.e6. https://doi.org/10.1016/j.neuron.2017.05.037.

71. Vasek, M.J., Garber, C., Dorsey, D., Durrant, D.M., Bollman, B., Soung, A., Yu, J., Perez-Torres, C., Frouin, A., Wilton, D.K., et al. (2016). A complement–microglial axis drives synapse loss during virus-induced memory impairment. Nature *534*, 538–543. https://doi.org/10.1038/nature18283.

72. Tesco, G., and Lomoio, S. (2022). Pathophysiology of neurodegenerative diseases: An interplay among axonal transport failure, oxidative stress, and inflammation? Semin. Immunol. *59*, 101628. https://doi.org/10.1016/j.smim.2022.101628.

73. Arrázola, M.S., Saquel, C., Catalán, R.J., Barrientos, S.A., Hernandez, D.E., Martínez, N.W., Catenaccio, A., and Court, F.A. (2019). Axonal Degeneration Is Mediated by Necroptosis Activation. J. Neurosci. *39*, 3832–3844. https://doi.org/10.1523/jneurosci.0881-18.2019.

74. Scarlett, J.M., Zhu, X., Enriori, P.J., Bowe, D.D., Batra, A.K., Levasseur, P.R., Grant, W.F., Meguid, M.M., Cowley, M.A., and Marks, D.L. (2008). Regulation of agouti-related protein messenger ribonucleic acid transcription and peptide secretion by acute and chronic inflammation. Endocrinology *149*, 4837–4845. https://doi.org/10.1210/en.2007-1680.

75. Nogueira, G., Solon, C., Carraro, R.S., Engel, D.F., Ramalho, A.F., Sidarta-Oliveira, D., Gaspar, R.S., Bombassaro, B., Vasques, A.C., Geloneze, B., et al. (2020). Interleukin-17 acts in the hypothalamus reducing food intake. Brain Behav. Immun. *87*, 272–285. https://doi.org/10.1016/j.bbi.2019.12.012.

76. Varela, L., and Horvath, T.L. (2019). Parallel Paths in PVH Control of Feeding. Neuron *102*, 514–516. https://doi.org/10.1016/j.neuron.2019.04.026.

77. Oh, J., Ontaneda, D., Azevedo, C., Klawiter, E.C., Absinta, M., Arnold, D.L., Bakshi, R., Calabresi, P.A., Crainiceanu, C., Dewey, B., et al. (2019). Imaging outcome measures of neuroprotection and repair in MS: A consensus statement from NAIMS. Neurology *92*, 519–533. https://doi.org/10.1212/WNL.0000000000007099.

78. Burfeind, K.G., Yadav, V., and Marks, D.L. (2016). Hypothalamic Dysfunction and Multiple Sclerosis: Implications for Fatigue and Weight Dysregulation. Curr. Neurol. Neurosci. Rep. *16*, 98. https://doi.org/10.1007/s11910-016-0700-3.

79. Genç, B., Şen, S., Aslan, K., and İncesu, L. (2023). Volumetric changes in hypothalamic subunits in patients with relapsing remitting multiple sclerosis. Neuroradiology *65*, 899–905. https://doi.org/10.1007/s00234-023-03122-z.

80. Huitinga, I., De Groot, C.J., Van der Valk, P., Kamphorst, W., Tilders, F.J., and Swaab, D.F. (2001). Hypothalamic lesions in multiple sclerosis. J. Neuropathol. Exp. Neurol. *60*, 1208–1218. https://doi.org/10.1093/jnen/60.12.1208.

81. Melief, J., de Wit, S.J., van Eden, C.G., Teunissen, C., Hamann, J., Uitdehaag, B.M., Swaab, D., and Huitinga, I. (2013). HPA axis activity in multiple sclerosis correlates with disease severity, lesion type and gene expression in normal-appearing white matter. Acta Neuropathol. *126*, 237–249. https://doi.org/10.1007/s00401-013-1140-7.

82. Faul, F., Erdfelder, E., Lang, A.-G., and Buchner, A. (2007). G*Power 3: A flexible statistical power analysis program for the social, behavioral, and biomedical sciences. Behav. Res. Methods *39*, 175–191. https://doi.org/10.3758/BF03193146.

83. Cellerino, M., Ivaldi, F., Pardini, M., Rotta, G., Vila, G., Bäcker-Koduah, P., Berge, T., Laroni, A., Lapucci, C., Novi, G., et al. (2020). Impact of treatment on cellular immunophenotype in MS: A cross-sectional study. Neurol. Neuroimmunol. Neuroinflamm. *7*, e693. https://doi.org/10.1212/NXI.0000000000000693.

84. Vigo, T., Voulgari-Kokota, A., Errede, M., Girolamo, F., Ortolan, J., Mariani, M.C., Ferrara, G., Virgintino, D., Buffo, A., Kerlero de Rosbo, N., and Uccelli, A. (2021). Mesenchymal stem cells instruct a beneficial phenotype in reactive astrocytes. Glia *69*, 1204–1215. https://doi.org/10.1002/glia.23958.

85. Li-Sha, G., Xing-Xing, C., Lian-Pin, W., De-Pu, Z., Xiao-Wei, L., Jia-Feng, L., and Yue-Chun, L. (2017). Right Cervical Vagotomy Aggravates Viral Myocarditis in Mice Via the Cholinergic Anti-inflammatory Pathway. Front. Pharmacol. *8*, 25. https://doi.org/10.3389/fphar.2017.00025.

86. Vigo, T., Procaccini, C., Ferrara, G., Baranzini, S., Oksenberg, J.R., Matarese, G., Diaspro, A., Kerlero de Rosbo, N., and Uccelli, A. (2017). IFN-γ orchestrates mesenchymal stem cell plasticity through the signal transducer and activator of transcription 1 and 3 and mammalian target of rapamycin pathways. J. Allergy Clin. Immunol. *139*, 1667–1676. https://doi.org/10.1016/j.jaci.2016.09.004.

87. Schiavi, S., Petracca, M., Sun, P., Fleysher, L., Cocozza, S., El Mendili, M.M., Signori, A., Babb, J.S., Podranski, K., Song, S.-K., and Inglese, M. (2021). Non-invasive quantification of inflammation, axonal and myelin injury in multiple sclerosis. Brain *144*, 213–223. https://doi.org/10.1093/brain/awaa381.

88. Risso, D., Ngai, J., Speed, T.P., and Dudoit, S. (2014). Normalization of RNA-seq data using factor analysis of control genes or samples. Nat. Biotechnol. *32*, 896–902. https://doi.org/10.1038/nbt.2931.

89. Bullard, J.H., Purdom, E., Hansen, K.D., and Dudoit, S. (2010). Evaluation of statistical methods for normalization and differential expression in mRNA-Seq experiments. BMC Bioinf. *11*, 94. https://doi.org/10.1186/1471-2105-11-94.

90. Wu, T., Hu, E., Xu, S., Chen, M., Guo, P., Dai, Z., Feng, T., Zhou, L., Tang, W., Zhan, L., et al. (2021). clusterProfiler 4.0: A universal enrichment tool

for interpreting omics data. Innovation *2*, 100141. https://doi.org/10.1016/j.xinn.2021.100141.

91. Subramanian, A., Tamayo, P., Mootha, V.K., Mukherjee, S., Ebert, B.L., Gillette, M.A., Paulovich, A., Pomeroy, S.L., Golub, T.R., Lander, E.S., and Mesirov, J.P. (2005). Gene set enrichment analysis: a knowledge-based approach for interpreting genome-wide expression profiles. Proc. Natl. Acad. Sci. USA *102*, 15545–15550. https://doi.org/10.1073/pnas.0506580102.

92. Martens, M., Ammar, A., Riutta, A., Waagmeester, A., Slenter, D.N., Hanspers, K., A Miller, R., Digles, D., Lopes, E.N., Ehrhart, F., et al. (2021). WikiPathways: connecting communities. Nucleic Acids Res. *49*, D613–D621. https://doi.org/10.1093/nar/gkaa1024.

93. Kanehisa, M., Furumichi, M., Tanabe, M., Sato, Y., and Morishima, K. (2017). KEGG: new perspectives on genomes, pathways, diseases and drugs. Nucleic Acids Res. *45*, D353–D361. https://doi.org/10.1093/nar/gkw1092.

STAR★METHODS

KEY RESOURCES TABLE

REAGENT or RESOURCE	SOURCE	IDENTIFIER
Antibodies for flow cytometry		
Pacific Blue anti-mouse Lineage cocktail	Biolegend	Cat# 133310; RRID: AB_11150779
PE/Cyanine7 anti-mouse Ly-6A/E	Biolegend	Cat# 108114; RRID: AB_493596
APC/Cyanine7 anti-mouse CD117	Biolegend	Cat# 105826; RRID: AB_1626278
APC anti-mouse CD135	Biolegend	Cat# 135310; RRID: AB_2107050
FITC anti-mouse CD34	BD Biosciences	Cat# 560238; RRID: AB_1645242
PE/Cyianine5 anti-mouse CD127	Biolegend	Cat# 135016; RRID: AB_1937261
CD11b-PE anti-mouse	Biolegend	Cat# 101208; RRID: AB_312791
APC anti-mouse Ly-6G	Biolegend	Cat# 127613; RRID: AB_1877163
Brilliant Violet 421 anti-mouse Ly-6C	Biolegend	Cat# 128032; RRID: AB_2562178
Brilliant Violet 510 anti -mouse CD45	Biolegend	Cat# 103137; RRID: AB_2561392
PerCP anti-mouse CD19	Biolegend	Cat# 115531; RRID: AB_893278
PE anti-mouse CD19	Biolegend	Cat# 115507; RRID: AB_313642
APC anti-mouse CD3	Biolegend	Cat# 100236; RRID: AB_2561456
Pacific Blue anti-mouse CD4	Biolegend	Cat# 100428; RRID: AB_493647
PE anti-mouse CD8a	Biolegend	Cat# 100708; RRID: AB_312747
Brilliant violet 510 anti-mouse CD25	Biolegend	Cat# 102041; RRID: AB_2562269
AlexFluor 488 anti-mouse Foxp3	Biolegend	Cat# 320012; RRID: AB_439748
APC/Cyanine7 anti-mouse CD8a	Biolegend	Cat# 100714; RRID: AB_312753
AlexFluor 647 **anti-mouse Foxp3**	Biolegend	Cat# 320013; RRID: AB_439749
Fitc CD184 (Cxcr4) anti-mouse	Miltenyi Biotec	Cat# 130-102-911; RRID: AB_2655754
APC Vio 770 anti-mouse CD3	Miltenyi Biotec	Cat# 130-119-793; RRID: AB_2751847
PerCP/Cy5.5 anti-mouse CD31	Biolegend	Cat# 102420; RRID: AB_10613644
PE anti-mouse CD73 Recombinant	Biolegend	Cat# 101703; RRID: AB_2941372
PECY7 anti-mouse Epcam	Thermo Fisher Scientific	Cat# 25-5791-80; RRID: AB_1724047
Anti-mouse B3AR antibody	Alomone Labs	Cat# AAR-017; RRID:AB_2039720
FITC anti human CD45	Biolegend	Cat# 982316; RRID: AB_2876779
PEanti-human CD34	Thermo Fisher Scientific	Cat# 12–034942; RRID: AB_1548680
Antibodies for other purpose		
Rabbit anti-mouseThyrosine hydroxylase antibody	Abcam	Cat# ab112; RRID: AB_297840
Rabbit Anti-mouse c-Fos antibody	Merk (Millipore)	Cat# ABE457; RRID: AB_2631318
Mouse anti-mouse AgRP antibody	Abcam	Cat# ab254558; RRID: AB_3076273
Goat anti-mouse AgRP antibody	Thermo Fisher Scientific	Cat# PA5-47831; RRID: AB_2608453
Rabbit anti-mouse VGAT cytoplasmic domain	Synaptic Systems	Cat# 131 002; RRID: AB_887871
Goat anti-Rabbit IgG (H + L) Cross-Adsorbed Secondary Antibody, Alexa Fluor™ 594	Thermo Fisher Scientific	Cat# a11012; RRID: AB_2534079
Donkey anti-Goat IgG (H + L) Cross-Adsorbed Secondary Antibody, Alexa Fluor™ 594	Thermo Fisher Scientific	Cat# A-11058; RRID: AB_2534105
F(ab')2-Goat anti-Mouse IgG (H + L) Cross-Adsorbed Secondary Antibody, Alexa Fluor 594	Thermo Fisher Scientific	Cat# a11020; RRID: AB_2534087

(*Continued on next page*)

Continued

REAGENT or RESOURCE	SOURCE	IDENTIFIER
F(ab')2-Goat anti-Rabbit IgG (H + L) Cross-Adsorbed Secondary Antibody, Alexa Fluor 488	Thermo Fisher Scientific	Cat# a11070; RRID: AB_2534114
AAVs	N/A	N/A
pAAV-hSyn-DIO-EGFP	Addgene	cat# 50457
pAAV-hSyn-DIO-hM4D(Gi)-mCherry	Addgene	cat# 44362
pAAV-hSyn-DIO-hM3D(Gq)-mCherry	Addgene	cat# 44361
Chemicals, peptides, and recombinant proteins		
CL 316,243 hydrate	Sigma-Aldrich	Cat# C5976
SR 59230A	Sigma-Aldrich	Cat# S8688
Capsaicin	Sigma-Aldrich	Cat# M2028
Clozapine *N*-oxide (CNO)	Bio-Techne	Cat# 4936
Incomplete Freund'adjuvant	Sigma-Aldrich	Cat# F5506
Mycobacterium tuberculosis	Difco	strain H37RA
Pertussis toxin	List Biological	Cat# 181
MOG 35-55	Espikem	Cat# EPK1
Lycopersicon Esculentum (Tomato) Lectin, fluorescein (FITC)	Thermo Fisher Scientific	Cat# L32478
4′,6-diamidino-2-phenylindole (DAPI)	Thermo Fisher Scientific	Cat# D1306
SITOX blue	Thermo Fisher Scientific	Cat# S11348
Vectashield	Vectorlabs	Cat# H-1200
Fluoromount™ mounting medium	Sigma-Aldrich	Cat# F4680
Liberase™ TM Research Grade 10mg	Roche	Cat# 5401135001
Collagenase type IV	Sigma-Aldrich	Cat# C4-BIOC
DNasi I	Roche	Cat# 10104159001
Normal Goat Serum	Thermo Fisher Scientific	Cat# 31873
Critical commercial assays		
Foxp3 Fix/Perm buffer set	Biolegend	Cat# 421403
L/D (fixable viability stain575V)	BD Biosciences	Cat# 565694
Fax Lysing solution	BD Biosciences	Cat# 349202
Lympholyte®-H Cell Separation Media	Euroclone	Cat# 5020-R
Mouse/Rat Noradrenaline ELISA	Eagle Biosciences	Cat# NOU39-K01 0
Human AGRP ELISA	Thermo Fisher Scientific	Cat# EHAGRP
BCA protein assay	Thermo Fisher Scientific	Cat# 55864
Luxol Fast Blue	Luxol Fast Blue	Cat# 04-200812
Qubit TM RNA HS Assay Kit	Thermo Fisher Scientific	Cat# Q32852
Qubit™ dsDNA HS Assay Kit	Thermo Fisher Scientific	Cat# Q32851
RNA ScreenTape	Agilent	Cat# 5067-5576
SuperScript® VILO™ cDNA Synthesis kit	Thermo Fisher Scientific	Cat# 11754050
Ion AmpliSeq™ Transcriptome Human Gene Expression Chef-Ready Kit	Thermo Fisher Scientific	Cat# A31446
Ion Chef TM system	Thermo Fisher Scientific	Cat# A27759
High Sensitivity DNA ScreenTape	Agilent Technologies	Cat# 5067-5584
Ion 540™ chip	Thermo Fisher Scientific	Cat# A27766
Fast start essential DNA green master	Roche	Cat# 06924204001
RNeasy micro kit	Qiagen	Cat# 74004
QuantiTect Reverse Transcription Kit	Qiagen	Cat# 205311
QIAzol Lysis Reagent	Qiagen	Cat# 79306

(*Continued on next page*)

Continued

REAGENT or RESOURCE	SOURCE	IDENTIFIER
Deposited data		
Mouse BM LSK cells RNA-sequencing	This paper	GSE214765 https://www.ncbi.nlm.nih.gov/geo/
Experimental models: Organisms/strains		
Mouse: C57BL/6	Envigo	N/A
Mouse: AgRP-TRPV1 (AgrpCreTm/+:Trpv1−/−:R26-LSL-Trpv1Gt/+)	Tamas Horvath, Yale University School of Medicine	Dietrich et al.[22]
Mouse: AgRP-ires-cre (*Agrp*$^{tm1(cre)Low/J}$)	The Jackson Laboratories	Strain # 012899
Oligonucleotides		
Actb Forward 5′-CTAAGGCCAACCGTGAAAAG-3′	This paper	N/A
Actb Reverse 5′-ACCAGAGGCATACAGGGACA-3′	This paper	N/A
Angpt1 Forward 5′-CTCGTCAGACATTCATCATCCAG-3′	This paper	N/A
Angpt1 Reverse 5′-CACCTTCTTTAGTGCAAAGGCT-3′	This paper	N/A
Agrp Forward 5′-AACTGCAGACCGAGCAGAAG-3′	This paper	N/A
Agrp Reverse 5′-AGACTCGCGGTTCTGTGG-3′	This paper	N/A
Bmp7 Forward 5′-GAAAACAGCAGCAGTGACCA-3′	This paper	N/A
Bmp7 Reverse 5′-GGTGGCGTTCATGTAGGAGT-3′	This paper	N/A
Cald Forward 5′-CGCAGAGAACTCAGGAGACAA-3′	This paper	N/A
Cald Reverse 5′-CATCATTTCTCTGATAGGCAATTC-3′	This paper	N/A
Cd3 Forward 5′-GATGCGGTGGAACACTTTCT-3′	This paper	N/A
Cd3 Reverse 5′-ACTGTCCTCGACTTCCGAGA-3′	This paper	N/A
Cxcl12 Forward 5′-CCAAACTGTGCCCTTCAGAT-3′	Méndez-Ferrer, S. et al.[4]	Méndez-Ferrer, S. et al.[4]
Cxcl12 Reverse 5′-ATTTCGGGTCAATGCACACT-3′	Méndez-Ferrer, S. et al.[4]	Méndez-Ferrer, S. et al.[4]
Gfap Forward 5′-TCGAGATCGCCACCTACAG-3′	This paper	N/A
Gfap Reverse 5′-GTCTGTACAGGAATGGTGATGC-3′	This paper	N/A
Kitl Forward 5′-CCCTGAAGACTCGGGCCTA-3′	This paper	N/A
Kitl Reverse 5′-CAATTACAAGCGAAATGAGAGCC-3′	This paper	N/A
Il-1β Forward 5′-GCCCATCCTCTGTGACTCAT-3′	This paper	N/A
Il-1β Reverse 5′-AGGCCACAGGTATTTTGTCG-3′	This paper	N/A
Il-7 Forward 5′-CGCAGACCATGTTCCATGT-3′	This paper	N/A
Il-7 Reverse 5′-TCTTTAATGTGGCACTCAGATGAT-3′	This paper	N/A

(*Continued on next page*)

Continued

REAGENT or RESOURCE	SOURCE	IDENTIFIER
Il-15 Forward 5′-AAGCCACTGGGTCTTTTCAA-3′	This paper	N/A
Il-15 Reverse 5′-TTCCAGACAGCCCGAGAG-3′	This paper	N/A
Lef1 Forward 5′-TCACTGTCAGGCGACACTTC-3′	This paper	N/A
Lef1 Reverse 5′-TGAGGCTTCACGTGCATTAG-3′	This paper	N/A
Prok2 Forward 5′-CCCCCTGACTCGGAAAAG-3′	This paper	N/A
Prok2 Reverse 5′-TCTTTCTTCTCTTCGCCCTTC-3′	This paper	N/A
Stat3 Forward 5′-GTTCCTGGCACCTTGGATT-3′	This paper	N/A
Stat3 Reverse 5′-CAACGTGGCATGTGACTCTT-3′	This paper	N/A
Stfa3 Forward 5′-CTCAAGTCGTTGCTGGACAA-3′	This paper	N/A
Stfa3 Reverse 5′-ATTGACGGCTGCATCTCTTT-3′	This paper	N/A
Thpo Forward 5′-GAGAATGGAAAACCCAGACG-3′	This paper	N/A
Thpo Reverse 5′-TCCCTCCAGTAGAAGGGACA-3′	This paper	N/A
Tnc1 Forward 5′-GCTGGTGCACCCAGAGAC-3′	This paper	N/A
Tnc1 Reverse 5′-ACAGTTGGATGTCCCCAATC-3′	This paper	N/A
Vcam Forward 5′-GACCTGTTCCAGCGAGGGTCTA-3′	This paper	N/A
Vcam Reverse 5′-CTTCCATCCTCATAGCAATTAAGGTG-3′	This paper	N/A
Zic2 Forward 5′-CCGAGAACCTCAAGATCCAC-3′	This paper	N/A
Zic2 Reverse 5′-CTTCCTGTCGCTGCTGTT-3′	This paper	N/A
Software and algorithms		
ImageJ	Fiji	https://imagej.net/software/fiji/
Prism 8	GraphPad Software	https://www.graphpad.com/scientific-software/prism/
NIS elements v4.50	Nikon	https://www.microscope.healthcare.nikon.com
FlowJo v10.8.1	BD Bioscences	https://www.flowjo.com/solutions/flowjo
MATLAB R2022b	MathWorks	https://it.mathworks.com
CellSens v 4.4	EVIDENT	https://evidentscientific.com/it/products/software/cellsens
G*power v3.1.9.7	Faul et al.[82]	http://www.gpower.hhu.de/

EXPERIMENTAL MODEL AND STUDY PARTICIPANT DETAILS

Mice

Mice used in the experiments were 8–10 weeks old from both male and female. C57BL/6 mice were purchased from Charles River. Transgenic AgRP-TRPV1 mice (AgrpCreTm/+Trpv1−/−R26-LSL-Trpv1Gt/+) were developed and kindly provided by Tamas

Horvath and colleagues, Yale University School of Medicine.[22] AgRP-ires-cre mice were purchased from Jackson Laboratories (*Agrp*$^{tm1(cre)Lowl}$/J). AgRP-hM3Dq[32] and AgRP-hM4Di[37] were obtained by AAVs stereotaxic injections in AgRP-ires-cre mice, as described below. All procedures involving animals were performed according to the guidelines of the Animal Ethical Committee and comply with Decreto Legislativo 4 marzo 2014, n. 26, legislative transposition of Directive 2010/63/EU of the European Parliament and of the Council of 22 September 2010 on the protection of animals used for scientific purposes. Mice were maintained under pathogen-free conditions and housed with no more than five animals per cage under standardized light-dark cycle conditions with *ad libitum* access to food and water. All efforts were made to minimize the number of animals utilized. The research protocols were approved by the Ethical Committee for Animal Experimentation of the IRCCS Ospedale Policlinico San Martino and by the Italian Ministry of Health (515/2020PR, 883/2017PR and 595/2022-PR). The clinical scores of each EAE experiment are reported in Figure legends and Figures 5N–5P, 6Q–6S, S1A, S11A and S13J.

Human subjects

This was a retrospective study conducted on blood samples of PwMS and HD recruited at the MS Outpatients Clinic of the IRCCS Ospedale Policlinico San Martino, Genoa, Italy. People participating in this study[83] provided signed informed consent to analysis aimed at identifying disease-related biomarkers, according to the research protocol approved by the regional ethical committee (CER Liguria: 100/2022 – DB id 12212). Inclusion criteria were: age 18–80 years; MS diagnosis according to the 2010 McDonald's criteria; relapsing-remitting or progressive course according to Lublin's criteria; disease duration $\leq$15 years for people with RRMS (no restriction with respect to disease duration for the PMS group). Exclusion criteria were: use of corticosteroids in the last 30 days, a relapse in the month prior to inclusion, impossibility of performing blood draw, chronic diseases other than MS, and pregnancy during the course of the study. Demographic and clinical data are reported in Table S2.

METHOD DETAILS

Study design

The objective of this study was to investigate the interplay between hypothalamic AgRP neurons and the SNS in the control of hematopoiesis and thymopoiesis in experimental MS. We induced EAE in C57BL/6 mice and we used multiparametric flow cytometry and bulk RNA sequencing to define the effect of disease induction on the adrenergic activation of the BM and thymus. To assess the involvement of B3ARs and AgRP neurons in the control of hematopoiesis and lymphopoiesis in EAE, we treated EAE-induced mice with a selective antagonist of B3ARs. We used transgenic AgRP-TRPV1 and AgRP-hM3Dq naive mice to investigate the effect of stimulation of AgRP neurons on hematopoiesis and lymphopoiesis. Through confocal microscopy and *in vivo* electrophysiology, we assessed the activation state of AgRP neurons in EAE. We used transgenic AgRP-EGFP mice to genetically label AgRP neurons, and AgRP-hM3Di mice to investigate the effect of inhibition of AgRP neurons on EAE. To translate our findings to the human disease, we quantified the frequency of CD34$^+$ cell in peripheral blood and the concentration of AgRP peptide in blood samples collected from healthy donors (HD) and pwMS (Table S2).

EAE and treatments

EAE was induced in 8/10-week-old mice as previously described.[84] Briefly, C57BL/6 mice, AgRP-TRPV1 or AgRP-hM3Di mice were injected subcutaneously with 200 μL of emulsion containing 200 μg myelin oligodendrocyte glycoprotein (MOG) peptide spanning amino acids 35–55 (MOG35–55) (Espikem) in incomplete Freund's adjuvant (Sigma-Aldrich), supplemented with 0.6 mg Mycobacterium tuberculosis (strain H37RA; Difco). In the CFA experiments, C57BL/6 mice received the same emulsion lacking the MOG peptide. Mice were injected in the tail vein with 400 ng pertussis toxin (List Biological) in 100 μL of phosphate buffer saline solution immediately and 48 h after the immunization. Naive or EAE-induced C57BL/6 mice were daily administered via oral gavage with the B3AR antagonist SR59230A (2 mg/kg/die in phosphate-buffered saline (PBS) containing 1% DMSO, Sigma Aldrich) or injected intraperitoneally with the B3AR agonist CL316.243 (0.5 mg/kg/die in PBS, Sigma Aldrich). Naive AgRP-TRPV1 mice were injected intraperitoneally with CAPS (10 mg/kg/die in 200 μL of PBS containing 3.3% Tween 80, Sigma Aldrich) and/or with B3AR antagonist SR59230A (2 mg/kg/die in 100 μL PBS containing 1% DMSO, Sigma Aldrich) daily for 3 days. Control mice were injected with the same volume of vehicle (200 μL of PBS containing 3.3% Tween 80 or 100 μL PBS containing 1% DMSO, respectively). Naive AgRP-hM3D(Gq) and EAE-induced AgRP-hM3Di mice were administered daily with vehicle (PBS) or CNO (5mg/Kg) by oral gavage.

Neuropathology analysis of EAE

Mice were sacrificed at 15 dpi. Animals were deeply anesthetized and transcardially perfused with phosphate-buffered 4% paraformaldehyde (PFA). Following perfusion, the lumbar segment of the spinal cord was carefully extracted via laminectomy, post-fixed in 4% PFA for 2 h at 4°C, then dehydrated and embedded in paraffin. Serial 14 μm-thick sections were cut using a rotary microtome and mounted on glass slides for histological analysis. Paraffin sections were stained with hematoxylin and eosin (H&E) to assess inflammatory infiltrates, and with Luxol Fast Blue (LFB) to evaluate the extent of demyelination. For H&E, staining followed standard protocols (hematoxylin 10 min + eosin 3 min) while LFB staining was performed according to the manufacturer's kit instructions (Bio-optica). All images were acquired using bright-field microscopy under standardized acquisition settings and quantitative analysis was conducted on lumbar spinal cord sections (L1–L6 segments). Inflammatory infiltration was assessed on H&E-stained sections

by calculating the ratio of infiltrated area to the total of non-infiltrated parenchyma, expressed as a percentage. Demyelination was evaluated on LFB-stained sections by measuring the demyelinated area relative to the total section area, also expressed as a percentage. Image analysis was performed using ImageJ (NIH, USA) all measurements were carried out by two independent observers blinded to group allocation.

Viral injection

Six-to eight-week-old male and female AgRP-ires-cre homozygous mice underwent stereotaxic surgery for visualization and/or manipulation of AgRP neurons. Mice were anesthetized with isoflurane and placed in a stereotaxic frame (Stoelting, Wood Dale, IL, USA). Analgesia was achieved via subcutaneous injection of buprenorphine (0.1 mg/kg). A heating pad was placed underneath to maintain body temperature at 37°C during surgery. Eye dehydration was prevented by frequent topical application of eye drops. The head was first shaved and disinfected with Betadine before the skin incision. After bregma and lambda were aligned, two small holes were drilled into the skull using a dental drill at the following coordinates from bregma: AP −1.7 mm; DV −5.1 mm; ML ±0.4 mm. 300 nL of pAAV-hSyn-DIO-EGFP, pAAV-hSyn-DIO-hM4D(Gi)-mCherry, or pAAV-hSyn-DIO-hM3D(Gq)-mCherry were purchased from Addgene and injected at 1 nL/s using a glass pipette connected to a Nanoject II (Drummond Scientific Company). Animals recovered for three weeks after surgery before starting subsequent procedures.

Surgery

Transection of sciatic and femoral nerves was performed as previously described.[5]

Unilateral cervical vagotomy was performed as previously described.[85] Ten days after surgery, mice were induced for EAE. Sham-operated mice were used as controls.

NE quantification

Tissues were homogenized in 0.01 N HCl in the presence of 0.15 mM EDTA and 4 mM sodium metabisulfite. NE was quantified with an ELISA assay (Eagle Biosciences), according to the manufacturer's instructions. The concentration of NE was normalized to the concentration of total protein evaluated by BCA protein assay (ThermoFisher Scientific).

Flow cytometry

BM was flushed out with PBS through femur bones, and cells were filtered through a 70μm cell strainer. For thymocytes analysis, cells were collected by pressing with the plunger of a syringe on a 70-μm cell strainer, and Foxp3 intracellular staining was performed using Foxp3 Fix/Perm buffer (Biolegend). For thymus epithelial cells analysis, thymic lobes were cut into small fragments and enzymatically digested using Liberase 0.05 %w/v (Roche), collagenase IV 0.25 mg/mL (Sigma-Aldrich) and DNase I 0.1 mg/mL (Roche) at 37°C in a CO_2 incubator for 30 min. Blood samples from mice were lysed by using Facs Lysing solution (BD Biosciences), labeled and then fixed. PBMCs were isolated from peripheral blood of pwMS and HD by Lympholyte-H density gradient centrifugation media (Euroclone). Cells were resuspended in PBS containing 1% bovine serum albumin (BSA) and 2 mM EDTA and labeled with fixable viability stain 575V (BD Biosciences) for dead cells exclusion. The antibodies used are listed in STAR Methods. Cells were analyzed with a cytometer (FACS CytoFLEX, Beckman Coulter) and the FlowJo software (BD Biosciences). The gating strategies are shown in Figures S2A, S2B, S4B, S4C, S8A and S9A.

Confocal and fluorescence microscopy

Femurs were dissected and fixed in 4% paraformaldehyde (PFA) for 24 h. Femoral bones were decalcified in 10% EDTA under constant rotation for 3 days, then included in low-melting agarose and sectioned in 400-μm-thick slices using a vibratome. Free-floating slices were labeled with a rabbit anti-mouse TH antibody (1:100, Abcam) for 24 h under constant agitation at 4°C, followed by a 2-h incubation with a secondary Alexa Fluor 594 conjugated antibody (ThermoFisher Scientific), and counterstained with fluorescein isothiocyanate (FITC)-conjugated tomato lectin (ThermoFisher Scientific), and with 4′,6-diamidino-2-phenylindole (DAPI, ThermoFisher Scientific) to label blood vessels and cell nuclei, respectively. Slices were analyzed with a Nikon A1 laser scanning confocal microscopy equipped with 405nm, 488nm and 561 nm CW lasers. TH + fibers were counted on three images for each femur using ImageJ.

Thymuses were harvested from mice perfused with PBS EDTA 2nM, washed in PBS and fixed with PFA 4%. Thymuses were then embedded in paraffin. Immunostaining of adrenergic fibers was performed in 50 μm slices. After deparaffinization and hydration, the slices were blocked with 10% Normal Goat Serum in PBS for 30 min. The thymic slices were then incubated overnight at 4°C with anti-tyrosine hydroxylase antibody (1:100, Abcam) in 10% NGS in PBS, followed by a 2-h room temperature (RT) incubation with the secondary antibody Alexa Fluor 488 IgG goat anti-rabbit (1:1000, ThermoFisher Scientific) in 10% NGS in PBS. After washing, vessels were stained using tomato lectin 594 (1:1000, Vector Laboratories) RT for 2 h. Slices were then extensively washed in PBS. Cell nuclei were stained with 10 nM SITOX Blue (ThermoFisher Scientific) for 15 min, and mounted on cover glass using Fluoromount medium (Sigma-Aldrich). Immunostaining of B3ARs was performed in 5 μm slices. After deparaffinization and hydration, slices were blocked with 5% BSA in PBS for 30 min and then incubated overnight at 4°C with the anti-β3-adrenergic receptor primary antibody (1:20, Alomone Labs) in 5% BSA in PBS, followed by a 2-h RT incubation with the secondary antibody Alexa Fluor 488 IgG goat anti-rabbit (1:1000, ThermoFisher Scientific) in 5% BSA in PBS. Slices were then extensively washed in PBS. Cell nuclei were then stained with 10 nM SITOX Blue (ThermoFisher Scientific) for 15 min and slices were mounted on coverslips using Fluoromount medium

(Sigma-Aldrich) and sealed with nail polish. Slides were acquired using a Leica Stellaris 8 Tau-STED microscope (Leica Microsystems, Mannheim, Germany).

Brains were isolated upon mice perfusion with 4% PFA and post-fixed overnight in 4% PFA, then embedded in 30% sucrose for 24–48 h. Slices of 50-μm thickness were sectioned using a cryostat. Brain slices were labeled with anti-mouse AgRP (1:100, Thermo Fisher Scientific or 1:500, Abcam), c-Fos (1:1000, Abcam) and vGAT (1:600, Synaptic System) antibodies overnight at 4°C, followed by 45-min incubation with the appropriate secondary Alexa Fluor-conjugated antibodies (ThermoFisher Scientific), and counterstained with DAPI (Thermo Fisher Scientific). Images were acquired with an IXplore IX83 SpinSR microscope, a 40x or 60× objective, and cellSENS dimension software, keeping acquisition parameters constant for each channel across samples (intensity of the fluorescent lamp, exposition time and gain). For VGAT staining in the PVH, a stack of images (5 μm; 10 z-stacks) from the surface of the stained slice was acquired. The resulting images (16-bit, 1.4 × 0.94 mm, 0.1625 μm/pixel) were saved in VSI format and imported into ImageJ (NIH) for analysis. For analysis of AgRP intensity, regions of interest (ROIs) were manually identified for each side around the ARC and PVH areas defined by the high AgRP immunoreactivity and measured for mean fluorescence intensity, following image background subtraction. At least 6 subsequent brain slices per mouse were analyzed.

For the analysis of c-FOS$^+$ nuclei, an automatic threshold was applied using the Otsu algorithm on the c-FOS fluorescence channel. Within each ROI, particle analysis was performed using the Analyze Particles function in FIJI/ImageJ, with a minimum particle size of 400 pixels and circularity set between 0.03 and 1.00 to exclude any fluorescence events with unsuitable size or shape. The results were expressed as the number of c-FOS$^+$ nuclei per ROI area (in mm^2), normalizing the data based on the surface area of each ROI for each brain slice**.** To quantify AgRP neurons projections (labeled by EGFP via viral injections) in the PVH, measurements were performed on three single planes of the z stack (0.5 μm; 2 μm distance between each other). ROIs were manually defined and the area in the PVH innervated by AgRP neurons was measured. To account for the variability of viral injection efficiency, this area was normalized to the number of infected neurons in the ARC, measured by manual counting of EGFP+ cells. To quantify VGAT-positive signal only within AgRP projections in the PVH, we first thresholded the EGFP signal to generate a binary mask representing AgRP axons (Figure 6H, Binary EGFP panel) and was then intersected with the VGAT staining (Figure 6H, Binary EGFP/VGAT panel). The resulting area of co-localization (VGAT$^+$ within EGFP$^+$ axons) was measured and normalized to the total slice area. This approach allowed us to isolate and quantify VGAT expression specifically within AgRP axons, thereby excluding inhibitory input from other sources. At least 8 subsequent brain slices per mouse were analyzed.

Primary cultures of bone marrow-derived MSCs[86] were fixed in 4% PFA, permeabilized with 0.5% Triton, and labeled with an anti-mouse B3AR primary antibody (1:50, Alomone Labs) in 3% BSA in PBS overnight at 4°C, followed by a 2-h RT incubation with a goat anti-rabbit (H + L) IgG cross-adsorbed secondary antibody conjugated with Alexa Fluor 594 (1/5000, ThermoFisher Scientific) in 3% BSA in PBS. Cell nuclei were stained with 10 nM SITOX Blue (ThermoFisher Scientific) for 15 min. The slides were mounted on coverslips using Fluoromount medium (Sigma-Aldrich) and acquired using a Leica Stellaris 8 Tau-STED microscope, using an HC PL APO CS2 100x/1.40 oil immersion objective lens (Leica Microsystems, Mannheim, Germany).

Real-Time PCR

Total RNA of bone marrow, thymus and hypothalamus from both C57BL/6 mice and AgRP-TRPV1 mice, was extracted with QIAzol Lysis Reagent (Qiagen), according to the manufacturer's instructions. Reverse transcription was performed with QuantiTect Reverse Transcription Kit (Qiagen). Real-time PCR experiments were conducted as per the manufacturer's instructions (Fast start essential DNA green master, Roche) using the LightCycler 480 Real-Time PCR system (Roche). Gene expression levels were normalized to actin B (Actb) as a validated reference gene and reported as fold change relative to a control condition using 2(-ΔΔCT) methods, except where differently indicated.

In vivo extracellular recordings

Naive and EAE-induced (7 dpi) AgRP-TRPV1 mice were anesthetized with xylazine (5 mg/kg) and ketamine (50 mg/kg) and placed in a stereotaxic frame (Stoelting Co.) for craniotomy. A hole in the skull, corresponding to the position of Arc was drilled (stereotaxic coordinates: 1.7 mm from the intersection between the sagittal and lambdoid sutures, 0.40 mm from lateral and ∼5.2 mm ventral to brain surface). After exposure of the brain surface, the dura mater was gently removed, and a glass pipette was used for *in vivo* extracellular recordings. Mice were recorded for 30 min before and 1 h after the intraperitoneal injection of CAPS. Extracellular signals were amplified and band-pass filtered (1–3000 Hz) by a NeuroLog system (Digitimer Ltd, Welwyn Garden City, UK) and finally digitized through a multifunction I/O device (NI USB-6251; National Instrument Co., Austin, TX). Mice were maintained under anesthesia during the experiments, and reflexes and body temperature (36°C) were monitored and kept stable. After recordings, mice were euthanized, and brains were collected for immunohistochemical analysis.

Firing rate analysis

Extracellular signals were high-pass filtered (500 Hz), and spike detection was set above 4-fold the standard deviation (SD) of the baseline. The average of the highest firing rate (5-s bins) before and after the intraperitoneal injection of CAPS was measured. Data analysis was carried out using the MATLAB R2022b software.

RNA sequencing

Lin$^-$/Sca-1$^+$ cells were isolated by cell sorting from the BM of mice immunized for EAE and treated or not daily with the B3AR antagonist SR59230A, as described above. Total RNA was extracted using RNeasy micro kit (Qiagen) and quantified by Qubit TM RNA HS Assay Kit (ThermoFisher Scientific). RNA integrity was evaluated using RNA ScreenTape on Tapestation 2200 System (Agilent Technologies). For library preparation, RNA (10 ng) was reverse-transcribed using the SuperScript VILO cDNA Synthesis kit (ThermoFisher Scientific). cDNA was amplified using Ion AmpliSeq Transcriptome Human Gene Expression Chef-Ready Kit (ThermoFisher Scientific) that allows simultaneous gene expression measurement of over 20,000 human Refseq genes. Barcoded libraries were prepared with Ion Chef TM system (ThermoFisher Scientific). Library size was checked using High Sensitivity DNA ScreenTape (Agilent Technologies) on Tapestation 2200 instrument, and library concentration was evaluated with a Qubit 2.0 Fluorometer using Qubit dsDNA HS Assay Kit. Amplified barcoded libraries were pooled and diluted to 50 pM for template preparation, and sequenced on an Ion 540 chip (ThermoFisher Scientific) on the Ion S5 System, according to the manufacturer's protocol.

AgRP neuropeptide quantification

AgRP neuropeptide was quantified in serum samples by using an ELISA assay (ThermoFisher Scientific), according to manufacturer's instructions.

Brain MRI

PwMS underwent brain MRI at 3.0 Tesla scanners (Siemens Prisma) with 36-channel head coil and with the following sequences: (a) sagittal three-dimensional (3D) fluid-attenuated inversion recovery (FLAIR); (b) sagittal 3D T1-weighted. FLAIR- and T1-weighted lesion volume was performed in each patient by a single experienced observer unaware of subject identity, using a segmentation technique based on user-supervised local thresholding (Jim 7.0, Xinapse System; http://www.xinapse.com) as previously described.[87]

QUANTIFICATION AND STATISTICAL ANALYSIS

RNA-seq analysis was performed in the R environment. Raw counts were imported using the edgeR package. Scaling of raw library size was used to calculate normalization factors, whereas unwanted variation between sample counts was removed using the RUVr method of Risso et al.[88] with two factors of unwanted variation in the model. The normalization method used was upper quartile,[89] in which the scale factors are calculated from 75% quantile of the counts for each library. DEGs were calculated by fitting a negative binomial generalized log-linear model after estimating common negative binomial dispersion as well as gene-wise empirical Bayes estimation of the negative binomial dispersion. Overrepresentation and gene set enrichment analyses for the various analysis contrasts were performed using the clusterProfiler package.[90] Gene sets were obtained from MSigDB (v.7),[91] whereas pathways were retrieved from wiki Pathways[92] and KEGG.[93] Uninominal *p*-values, as well as Benjiamini-Hochberg (FDR) multiple testing-corrected values are reported for each analysis. Due to the exploratory nature of our transcriptomic experiments, we also took into consideration DEGs deemed of biological relevance, but which did not pass formal significance thresholds after multiple testing correction. However, to ensure that those were not falsely positive results, we validated their differential expression in independent experiments by Real-Time PCR.

For the other datasets, statistical analysis and data visualization were performed using the Prism 8 software (GraphPad Software). Power analysis and sample size calculations were performed using G*Power software.[82] All analysis was performed by investigators blinded to the experimental groups. All experiments presented in this study were repeated at least twice. Normal distribution was assessed using the D'Agostino-Pearson's normality test. The unpaired Student's *t*-test was used to compare two normally distributed sample groups; one-way ANOVA followed by Tukey's multiple comparisons test or two-way ANOVA followed by Dunnet's multiple comparisons test was used to compare more than two normally distributed sample groups. The Mann-Whitney *U*-test was used to compare more than two non-normally distributed groups; R-squared test was applied in a regression model. Log -rank test was used to compare the survival distributions of two groups. Alpha levels for all tests were 0.05%. Statistical details about n number and *p* value were reported in Figure legends.